



This is to certify that the

dissertation entitled NERNST-ETTINGSHAUSEN MEASUREMENTS ON ALUMINUM BELOW 1K

presented by

Ahmad Amjadi

has been accepted towards fulfillment of the requirements for

Ph. D. degree in Physics

Major professor

Date 3-18-86



RETURNING MATERIALS:
Place in book drop to remove this checkout from your record. FINES will be charged if book is returned after the date stamped below.

NERNST-ETTINGSHAUSEN MEASUREMENTS ON ALUMINUM BELOW 1K

Ву

Ahmad Amjadi

A DISSERTATION

Submitted to

Michigan State University

in partial fulfillment of the requirements

for the degree of

DOCTOR OF PHILOSOPHY

Department of Physics

1986

ABSTRACT

NERNST-ETTINGSHAUSEN MEASUREMENTS ON ALUMINUM BELOW 1K

By

Amjadi Ahmad

We have constructed a system for transport measurements below 1K in magnetic fields up to 30kG, and used it to measure the high magnetic field limit of the Nernst-Ettingshausen coefficient for a pure polycrystalline Aluminum sample at 210mK, where we expect phonon-drag contributions to be negligible. Previous measurements on Al were limited to above 1.8K. Our data indicate that the electron-phonon mass enhancement continues to appear in the off-diagonal component of the thermoelectric tensor coefficient at temperatures well below 1K. To within our measuring uncertainty, the enhancement in our data between 10 kG and 20 kG is consistent with $(1+\lambda_0)$, in agreement with the low-temperature, high-field NE coefficient measurements of Al from 1.8K to 5K by Thaler, Fletcher and Bass (ref.3). The data are less consistent with an alternative prediction of $(1 + 2/3\lambda_0)$.

As shown in Figure (4.2), above 20 kG the measured values of the NE coefficient start to drop from the saturated value at lower fields (i.e. between 10 kG and 20 kG). This effect is most likely due to magnetic breakdown in Al above 20 kG. By taking closely spaced data points from 20 kG to 30 kG, we looked for evidence of the quantum oscillations which accompany such breakdown in the thermopower of single crystal samples (ref.8). However, no convincing evidence of such oscillations was found. We assume that their absence is due to the polycrystalline nature of our sample.

TO MY WIFE

ACKNOWLEDGEMENTS

It is a great pleasure to acknowledge my thesis advisor Professor Jack Bass, whose suggestions and criticisms throughout the course of this research were invaluable. I would also like to thank Professor Pratt, Professor Schroeder and Professor Spence for their precious advice, discussions, and help at many stages of this study. Specific thanks go to Professor Foiles for his suggestions on Thermometer preparation.

I am indebted to Dr. Mark Haerle and Dr. Vernon Heinen for their unselfish help on different stages of this research. I would like to extend thanks to the good humored fellows in the machine shop for their help in constructing the precise centering device, sample can, high vacuum can, heat exchangers, and all the mechanical supports for the superconducting magnet, the Liquid Nitrogen and Helium dewars, and the sample.

Finally, the financial support of the National Science Foundation is gratefully acknowledged.

TABLE OF CONTENTS

Chap	ter	Page
LIST	OF TABLES	viii
LIST	OF FIGURES	ix
I.	INTRODUCTION	
	1.1 Introduction	01
	1.1.1 Transport Equations	02
	1.1.2 Compensated Metals	07
	1.1.3 Uncompensated Metals	80
	1.2 Previous Work	12
	1.3 Present Thesis	24
	1.3.1 Construction	24
	1.3.2 Thermoelectric Measurements of Aluminum	25
II.	EXPERIMENTAL TECHNIQUES	
	2.1 Introduction	28
	2.2 Dilution Refrigerator	28
	2.3 High Precision (0.1 PPM) Resistance Bridge	31
	2.4 SQUID	31
	2.5 Vibration Isolation of the Cryostat	32
	2.5.1 Magnet Supports	32
	2.5.2 Centering Device	33
	a. Stage 1, Thermal isolation	
	between the mixing chamber and	
	the 1.2K copper band heat exchanger	36

Chapter	Page
b. Stage 2, Thermal isolation	
between the copper band and the	
surrounding vacuum can	37
2.6 Thermometry in High Magnetic Field at	37
Low Temperature	
2.6.1 Different Thermometers	39
2.6.2 Thermometer Preparation	41
2.6.3 Thermometer Calibration	46
2.6.4 Temperature Regulation	48
2.7 Sample	
2.7.1 Sample Size	49
2.7.2 Sample Preparation	51
2.7.3 Annealing	51
2.7.4 Sample Connections	53
a. Electrical connections	53
b. Thermal connections	53
c. Mechanical connections	54
2.7.5 Electrical contacts to the sample	56
a. Spotwelding	56
b. Soldering Indium	57
c. Plating	58
2.7.6 Magnetic Field and Current Density	61
Dependence of Different Solders	
2.7.7 Sample Can	64
2.8 Superconductive Magnet	65
2.8.1 Introduction	65

..

Chapter	Page
2.8.2 Electrical connections to the Super-	
Conducting magnet	66
2.8.3 Pressure Relief Valves	67
2.9 Reference Resistor	70
2.10 SQUID's in a Feedback Loop	71
III. THEORY	75
3.1 Electron-Phonon Mass Enhancement	75
3.2 Fundamental Transport Theory	83
3.3 Transport in High Magnetic Field	88
3.4 The High Magnetic Field Nernst-Ettingshausen	95
Coefficient	
IV. THE EXPERIMENTS AND RESULTS	101
4.1 Temperature Range 1K to 4.2K	101
4.1.1 The Hall Coefficient ($R_{ m H}$) above 1K	101
4.1.2 The NE Coefficient above 1K	102
4.2 Measurements at Temperatures below 1K	103
4.2.1 The Hall Coefficient ($R_{ m H}$) below 1K	103
4.2.2 The NE Coefficient measurements below 1K	107
4.2.3 Correction of Q_{χ} by R_{L} Measurements	108
4.3 Conclusion	113
REFERENCES	115
APPENDIX A	118

LIST OF TABLES

Table		Page
(1.1):	Comparison of Calculated and Experimental	13
	Effective Masses in Na, Al, Pb.	
(4.1):	${\mathtt R}_{f H}$ for Pure Aluminum Sample at Different	105
	Magnetic Fields and a Constant Temperature	
	147 mK.	
(4.2):	Nernst-Ettingshausen Coefficient Measure-	110
	ments for Different Values and Direction	
	("z"-direction and "-z"-direction) of the	
	Magnetic Field from Direct Measurements and	
	Corrected Values using $R_{f L}$ Coefficient	
	Measurements.	

. .

LIST OF FIGURES

Figure		Page
(1.1)	$\frac{P^a}{B}$ as a Function of Magnetic Field B for	20
	Temperatures 2.3K and 4.6K.	
(1.2.a,b)	$\frac{P^a}{B}$ as a Function of T^2 (a) and T^3 (b) for	20
	Magnetic Fields of 1.5 $T(\Delta)$, 1.8 $T(\Box)$,	
	2.0 T(o) and 2.1 T(). The broken lines	
	indicate the value predicted from the	
	electronic specific heat γ^{c} , which contains	
	the enhancement factor (1 + λ).	
(2.1)	Diagram of the Sample, inside the super-	30
	conducting Magnet, with the connections	
	between the mixing chamber and the	
	vacuum can through the centering device.	
(2.2)	Cross section view of the centering device.	35
	A-Brass Band. B-Copper Band Heat Exchanger.	
	C-The Upper Side of the Mixing Chamber.	
	D-Vespel Cylinder (stage 1 of the thermal	
	isolation). E-Vespel Cylinder (stage 2 of the	
	thermal isolation). F-Stainless Steel Rod.	
	G-Adjusting Screw. H-Locking Nut. I,J-Attaching	
	Screws.	

Figure		Page
(2.3)	Block diagram of the two stages of thermal	38
	isolation of the centering device. Stage 1-The	
	thermal isolation between the mixing chamber and	
	the copper band connected to the 1.2K heat	
	exchanger. Stage 2-The thermal isolation	
	between the copper band and the surrounding	
	vacuum can.	
(2.4)	Speer Carbon Thermometer: A-Speer Carbon Resistor	43
	Body. B-Speer Graphite. C-Superconducting NbTi	
	Leads. D-Copper Clad is removed from the super-	
	conducting wire. E-Silver paint for electrical	
	contacts between the leads and the speer carbon	
	thermometer. F-Superconducting wire with the	
	electrical insulation removed from it.	
(2.5)	Sample Holder: A-Main copper support. B-Pb	45
	shield for sample transverse voltage wires.	
	C-Heater leads. D-Heater. E-Heater stand.	
	F-Aluminum sample. G-Vespel substrate. H-	
	Thermometer. I-Thermometer holding-spring.	
	J-Current leads to the sample.	
(2.5.b)	Admitance of T _c as a Function of Temperature	47
	in Magnetic Fields; 15, 20, 25, kG.	
(2.6)	Brass sample cutter cross section.	52

Figure

(2.7)	Schematic	diagram	of the	electrical	circuit	55
	containing	the Al	sample	for Nernst	Ettingshausen	
	and Hall o	oeffici	ent mea:	surements.		

- (2.8.a) Schematic diagram of the set up for magnetic 62
 field and current density dependance studies of
 different solders. (A)-Electrical connections out
 of the magnetic field. (B)-Solder under test inside
 the magnetic field. M-Voltage and current leads.
 N-Electrical contacts. O-Superconducting leads.
 P-Pb tube. U-Sample can. Q-Superconducting magnet.
 R-Solder under test. S-Helium dewar. T-Liquid
 Helium.
- (2.8.b) Magnetic Field Distribution. 62
- (2.9) A-The magnetic field dependence of the contact 63 resistance. B-The current density dependence of the contact resistance a) Woods metal, b) Sn,
 c) Roses Alloy, d) In, e) Pb.
- (2.10) Helium pressure relief valve: A-Weight holder 69 screw. B-Extra weights. C-Top flange. D-Top valve holder. E-O-ring seal. F-Elbow. G-Brass pipe. H-Copper pipe casing.
- (2.11) Simplified block diagram of the SQUID circuit 73 in a feedback loop, for measuring i-switch position (A), Hall coefficient ii-switch position (B), Nernst Ettingshausen coefficient.

¥

Figure		Page
(3.1)	Electronic density of states as a function of	80
	energy, where $N_c^{(E)}$ and $N_c^{(O)}$ are the enhanced	
	and unenhanced electronic density of states.	
(3.2)	The dispersion relation, E(k) for enhanced and	81
	${\rm E_{0}}(k)$ for unenhanced electrons. The enhancement	
	has the effect of producing a different slope in	
	the vicinity of $E_{\hat{f}}$.	
(4.1)	Hall coefficient of Al as a function of	106
	magnetic field B at temperature 0.147K. The	
	broken line is the value predicted from the	
	known electronic structure of Al.	
(4.2)	Nernst-Ettingshausen coefficient of Al as a	112
	function of magnetic field at temperature	
	0.147 K. The broken line indicates the value	
	predicted from the electronic specific heat γ^c .	

CHAPTER I

I. INTRODUCTION

(1.1 Introduction).

Transport properties of metals have been studied over the years by numerous investigators, because they provide information about the physics of the materials. In recent years, the introduction of SQUIDs (superconducting quantum interference devices (Ref.1)) has greatly enhanced the sensitivity of low temperature transport measurements and has allowed considerable improvements in our understanding of different scattering processes, such as electron-electron and electron-phonon scattering in metals. Magnetic fields have also been employed extensively to investigate the magneto-transport properties in metals. However, due to the extreme sensitivity of SQUIDs to magnetic fields, it is difficult to use the powerful combination of SQUIDs plus magnetic field, particularly at ultra-low temperatures (T<1K) where the complexity of the low temperature apparatus inhibits proper shielding of the SQUID.

This dissertation is a report of the construction of a general purpose experimental system for carrying out high-magnetic field transport coefficient measurements using SQUIDs at ultra-low temperatures, and of the results of measurements of the off-diagonal diffusion component of the thermoelectric tensor $(\varepsilon''_{yx})_d$, of Aluminum below 1K. These measurements were used to test the system;

they are also of interest because this component is expected to be subject to a many-body renormalization involving the electron-phonon mass enhancement (λ).

In this introduction we start with a background on Transport equations and define the thermoelectric tensor and its components. Then we define the appropriate Nernst-Ettingshausen (NE) coefficients for compensated and uncompensated metals, and other coefficients such as the Hall coefficient and Righi-Leduc coefficient which are necessary for our experiment. We then review previous work on NE measurements, and finally, describe the present thesis and the reasons for measuring these coefficients on Aluminum at very low temperatures.

(1.1.1)TRANSPORT EQUATIONS:

The electrical and thermal current densities \vec{J} and \vec{U} are related to the electric field \vec{E} and the temperature gradient $\vec{\nabla}T$ by the fundamental transport equations (Ref. 2).

$$\begin{cases} \vec{J} = \vec{L}_{11} \vec{E} + \vec{L}_{12} (-\vec{\nabla}T) \\ \vec{U} = \vec{L}_{21} \vec{E} + \vec{L}_{22} (-\vec{\nabla}T) \end{cases}$$
(1.1)

$$L_{11}^{++} = \sigma^{+-}$$
 The electrical conductivity tensor

$$L_{12}^{++} = \varepsilon^{++} =$$
 The thermoelectric tensor

$$L_{21}^{++} = + \stackrel{\leftarrow}{\epsilon} = T \cdot \stackrel{\leftarrow}{\epsilon}"$$
 (1.3.a)

$$\dot{L}_{22} = + \dot{\lambda} = \dot{\lambda}'' + T \frac{\dot{\epsilon}''}{\dot{\sigma}}$$
 (1.3.b)

where

The thermal conductivity tensor.

All of these tensor coefficients are functions of magnetic field \vec{B} and temperature T. We focus primarily on the high-field limit of ϵ "_{yx}, the off-diagonal element of the thermoelectric tensor. This element is the sum of two terms, a diffusion component $(\epsilon$ "_{yx})_d and a phonon-drag component $(\epsilon$ "_{yx})_g (ref. 3)

$$\varepsilon'' yx = (\varepsilon'' yx)_d + (\varepsilon'' yx)_g$$
 (1.4)

As discussed in chapter III below, when \vec{B} is directed along an axis of at least 3-fold symmetry, the high-field limit of the diffusion component of the thermoelectric coefficient $(\epsilon''_{yx})_d$ for a metal which has no open orbits in the plane perpendicular to \vec{B} is just,

$$(\varepsilon''_{yx})_d = \pi^2 k^2 N_t(E_f) \frac{T}{3B}$$
 (1.5)

where

k = Boltzmann's constant

 $N_t(E_f)$ = The transport Electronic density of states at the Fermi energy E_f

T = Temperature (K)

B = Magnetic field (Tesla)

As we will see later in this introduction, $N_t(E_f)$ is expected to be enhanced by the electron-phonon mass enhancement (λ).

The high-field limit of the Phonon-drag component of the thermoelectric coefficient is

$$(\varepsilon''_{VX})_g = C \frac{T^\alpha}{B}$$
 (1.6)

where C is a constant which depends upon the metal of interest, and $\alpha \sim 3$, Opsal (Ref. 4). In 1968 Blewer et al (Ref. 5) argued that for a metal with a Debye Phonon spectrum, and neglecting electron-phonon-Umklapp scattering, the high-field limit of $(\epsilon"_{yx})_g$ should vary with temperature as T^3 . In 1977 Thaler et al (Ref. 3) suggested that even if the phonon spectrum were not Debye like, and electron-phonon Umklapp scattering were not negligible, one might hope that in equation (1.6) α is still much greater than one, so that the phonon-drag component $(\epsilon"_{yx})_g$ varies much more rapidly than the

electron-diffusion component $(\varepsilon''_{yx})_d$ as a function of temperature. In such a case $(\varepsilon''_{yx})_d$ can be separated from $(\varepsilon''_{yx})_g$ experimentally by means of their different temperature dependences as follows. Substitute equations (1.5) and (1.6) into (1.4) and multiply this equation by $\frac{B}{T}$. This gives:

$$\frac{\varepsilon''yx}{T} B = \pi^2 k^2 \frac{N_t(E_f)}{3} + C T^{(\alpha-1)}$$
 (1.7)

A plot of equation (1.7) against $T^{(\alpha-1)}$ where $(\alpha-3)$ should yield a straight line with intercept $\pi^2 k^2 \frac{N_t(E_f)}{3}$. In theory, this value of $N_t(E_f)$ could be compared with a calculated value to see whether it is enhanced. In practice, the enhancement for a given metal is rarely known well enough for accurate comparison. It is thus better to compare $N_t(E_f)$ with another experimental quantity which is known to be enhanced. This comparison is made by means of the electronic specific heat Υ^c , which is enhanced (Ref. 6) and which can also be written in terms of a density of states

$$\gamma^{c} = \pi^{2} k^{2} \frac{N_{c}(E_{f})}{3}$$
 (1.8)

Here N $_{c}(^{E}f)$ is the electronic density of states determined from measurements of γ^{c} .

For simplicity, let us call the intercept of equation (1.7) γ^{t}

$$\gamma^{t} = \pi^{2} k^{2} \frac{N_{t}(E_{f})}{3}$$
 (1.9)

where Y^t stands for "transport" specific heat.

Then we can write the high-field limit of the diffusion component of the thermoelectric coefficient as,

$$(\varepsilon''_{yx})_d = \gamma^c \frac{T}{B} (\frac{\gamma^t}{\gamma^c})$$
 (1.10)

Equation 1.10 tells us that measurement of $(\varepsilon''_{yx})_d$ provides a direct determination of the ratio γ^t/γ^c . Since γ^c is known to be enhanced, this ratio determines whether or not γ^t is enhanced. For example, the electron-phonon enhancement λ in Al is about 0.45. If γ^t is enhanced, the ratio γ^t/γ^c should be 1.0. If γ^t is not enhanced, the ratio should be 0.7.

With this background, let us see what are the best quantities to be measured in compensated and uncompensated metals in order to determine the diffusion component of the thermelectric coefficient $(\varepsilon''_{vx})_d$.

For simplicity, let us call the intercept of equation (1.7) γ^{t}

$$Y^{t} = \pi^{2} k^{2} \frac{N_{t}(E_{f})}{3}$$
 (1.9)

where Y^t stands for "transport" specific heat.

Then we can write the high-field limit of the diffusion component of the thermoelectric coefficient as,

$$(\varepsilon''_{yx})_d = \gamma^c \frac{T}{B} (\frac{\gamma^t}{\gamma^c})$$
 (1.10)

Equation 1.10 tells us that measurement of $(\epsilon'')_{yx}^{}_{$

With this background, let us see what are the best quantities to be measured in compensated and uncompensated metals in order to determine the diffusion component of the thermelectric coefficient $(\varepsilon''_{vx})_d$.

(1.1.2)Compensated Metals:

For a compensated metal the adiabatic Nernst-Ettingshausen (NE) coefficient Q^a is the most convenient experimental quantity from which to evaluate $\epsilon^{"}_{vx}$. Q^a is defined as

$$Q^{a} = \frac{-E_{y}}{\partial T/\partial x} = \frac{-(\Delta V_{y}/W)}{(\Delta T/\Delta x)}$$
(1.11)

where W is the sample width, E_y is the electric field produced in the y-direction when we apply the temperature gradient $\frac{\partial T}{\partial x} = \frac{\Delta T}{\Delta x}$ in the x-direction and a constant magnetic field \vec{B} in the z-direction. $\Delta V_y = E_y \cdot W$ is the voltage across the sample in the y-direction. The boundary conditions are $\vec{J} = 0$ and $U_y = U_z = 0$. (U_y and U_z are the heat flows per unit area in the y and z directions respectively).

In chapter III we will see that as B $\rightarrow \infty$ the diffusion component of Q^a, call it Q^a_d, reduces to;

$$Q_{d}^{a} = \varepsilon''_{yx} \rho_{yy} \qquad (1.12)$$

where ρ_{yy} is the electrical resistivity. We see from Equation 1.12 that measurements of Q_d^a and ρ_{yy} yield $\epsilon"_{yx}.$

For a compensated metal, the transverse electric field E_y is relatively large compared to an uncompensated metal. This makes ΔV_y fairly easy to measure. But on the other hand from equation (1.11) the NE coefficient measurement for a compensated metal requires the measurement of $\frac{\partial T}{\partial x}$ which is limited by accuracy in thermometery. Because accurate thermometry in high magnetic field and low temperature is not easy, if one has enough voltage sensitivity, uncompensated metals provide scope for more accurate determinations of Υ^t , as we will see next.

(1.1.3)Uncompensated Metals:

In an uncompensated metal the most convenient parameter for determining $\epsilon"_{\ VX}$ is the adiabatic NE coefficient defined as,

$$P^{a} = \frac{E_{y}}{U_{x}} \tag{1.13}$$

Here U_x is the applied heat flow per unit area in the x-direction, \vec{B} is in the z-direction, and the boundary conditions are again $\vec{J}=0$ and $U_y=U_z=0$.

In chapter III we will observe that as B $\rightarrow \infty$ the diffusion component of P^a, let us call it P^a_d approaches the value

$$P_d^a = \frac{\epsilon'' y x^{\rho} x x}{\lambda''' x y} = -\gamma^t \frac{B}{L_0 (n_e - n_h)^2 e^2}$$
 (1.14)

where L $_{\rm O}$ is the Sommerfeld-Lorenz number and n $_{\rm e}$ and n $_{\rm h}$ are respectively, the number of electrons and holes per unit volume in the metal.

Now from equation (1.13)

$$P^{a} = \frac{(\Delta V_{y}/W)}{(Q_{x}/t \cdot W)} = \frac{\Delta V_{y} \cdot t}{Q_{x}}$$
 (1.15)

where ΔV_y is the transverse voltage difference, Q_x is the total heat flow along the sample in the x-direction, and t and W are, respectively, the thickness and the width of the sample.

To discuss limitations, let us look at equation (1.15). At very low temperature $P^a \sim P_d^a$, where P_d^a is the diffusion component of the NE coefficient which has the high field limit shown in eq (1.14). Q_X is the total heat flow along the sample in the x-direction, which is limited by the power of the dilution refrigerator. Because the maximum power of the dilution refrigerator at very low temperature is limited, in order to have a significant transverse voltage ΔV_V , we need a very thin sample. But

a thin sample needs a substrate to hold it in the cryostat. Under these conditions two problems arise. The first problem is the measurement of the thickness (t) of a very thin sample at the cross section where $\mathbf{Q}_{\mathbf{X}}$ is measured, and the second one is the measurement of $\mathbf{Q}_{\mathbf{X}}$ (again at the same cross section where $\Delta \mathbf{V}_{\mathbf{Y}}$ is measured) along a sample which is attached to the substrate. Fortunately, there are cross-check measurements which allow these problems to be addressed.

i) The experimental check for the thickness t is the Hall coefficient

$$R_{H} = \frac{\rho_{yx}}{B} = \frac{E_{y}}{J_{x} \cdot B} = \frac{(\Delta V_{y}/W)}{\frac{I_{x} \cdot B}{W \cdot t}} = \frac{\Delta V_{y} t}{I_{x} \cdot B}$$
(1.16)

where ρ_{yx} is the transverse component of the electrical resistivity, J_x is the current density in the x-direction, I_x is the current in the x-direction. Since the Hall coefficient has the high-field limit (Ref. 2)

$$R_{H} = -\frac{1}{(n_{e} - n_{h})ec}$$
 (1.17)

which can be calculated from properties of the metal of interest, the thickness t can be calculated from equation (1.16)

$$t = -\frac{I_{x} \cdot B}{\Delta V_{y} (n_{e} - n_{h}) ec}$$
 (1.18)

ii) The experimental check for the thermal current along the sample $Q_{\mathbf{x}}$ is the Righi-Leduc R_L coefficient (ref. 7) which is defined as:

$$R_{L} = \frac{(\partial T/\partial y)}{Q_{x} \cdot B} = \frac{(\Delta T_{y}/W)}{Q_{x} \cdot B}$$
 (1.19)

where $\partial T/\partial y$ is the temperature gradient transverse to both the heat current $Q_{\mathbf{x}}$ and the magnetic-field \vec{B} , and $\Delta T_{\mathbf{y}}$ is the transverse temperature difference across the sample. $R_{\mathbf{L}}$ has a high field limit of,

$$R_{L} = \frac{1}{L_{o} T (n_{e} - n_{h}) ec} = -\frac{R_{H}}{L_{o} T}$$
 (1.20)

where L $_{\rm O}$ is the Lorenz number and T is the temperature. Measurement of R $_{L}$ and ΔT_{y} thus provides a cross-check on Q $_{x}.$

(1.2)Previous Work:

From 1956 to 1958, Landau (Ref. 9) shed a great deal of light on many-body interacting systems.

In 1964, Prange and Kadanoff (Ref. 10) extended the theory for electron-phonon interactions in metals to the nonequilibrium case, and asserted that the effect of electron-phonon mass enhancement was unobservable in dc electronic transport in metals. The above statement was proved microscopically for electrical conductivity in the same year by Holstein (Ref. 11), but not for thermal conductivity or thermoelectric effects.

In 1965, Ashcroft and Wilkins (Ref.12) reported that the low temperature electronic specific heat [equation (1.8)] is enhanced by electron-phonon and electron-electron interactions. To show this, they chose simple metals Na, Al and Pb because of their known Fermi surfaces and band structures. They compared experimental values of $\frac{m^*}{m}$ --extracted from low temperature electronic specific heat measurements in the literature --with their calculated $\frac{m^*}{m}$ taking into account band structure effects, electron-electron enhancements, and electron-phonon enhancement.

	Na	Al	Pb
$\left(\frac{m^*}{m}\right)_{BS}$	1.00	1.06	~1.12
$\left(\frac{\delta m}{m}\right)_{\text{el-el}}$	0.06	-0.01	0.00
$\left(\frac{\delta m}{m}\right)_{el-ph}$	0.18	0.49	1.05
$\left(\frac{m*}{m}\right)_{BS}\left[1+\left(\frac{\delta m}{m}\right)_{el-el}+\left(\frac{\delta m}{m}\right)_{el-ph}\right]$	1.24	1.57	2.30
$\left(\frac{m*}{m}\right)_{\text{exp}}$	1.25	1.45	2.00

(Table 1) Comparison of calculated and experimental effective masses in Na. Al. Pb.

Both the electron-electron enhancement and band structure effects were small compared to the electron-phonon enhancement. The experimental term $\frac{m^*}{m}$ for Aluminum was $\frac{m^*}{m}$ ~ 1.45, from which

$$m^* = m (1 + \lambda_0)$$
 (1.21)

gives a mass enhancement for Al of λ_{o} ~ .45.

In 1966, Grenier et al (Ref. 13) measured $\epsilon_{yx}^{"}$ of Cd in the He range. They found a value in the vicinity of the free electron value, but various uncertainties made them unable to determine the presence or absence of mass enhancement.

In 1968, Blewer et al (Ref. 14) extended the work done by Grenier and Long to lower temperature on Antimony for better understanding of the nature of the scattering mechanisms. They found Y^{t} to be 10-20% larger than Y^{c} . Because of uncertainties in the measurements, and the fact that the value of λ for Antimony was not known, this result also did not indicate whether there is an enhancement.

In 1970, Long (Ref. 15) measured the NE coefficient for a pure tungsten crystal in the temperature range of 1.4 - 4.1K and argued that the density of states computed from the NE coefficient was consistent with the values of specific heat measurements; in other words $\gamma^t = \gamma^c$. But the uncertainties in both values again made them unable to establish any enhancement.

In 1971, Averback and Bass (ref. 16) (see also Averback et al. ref. 17) measured the low-temperature magneto thermoelectric power of Al and a number of Al alloys and showed that the electron-diffusion component of S_d first became more positive as the magnetic field increased, and then saturated to a high field limit. They showed that the difference ΔS_d between the high field (B = ∞) and zero field (B = 0) values of S_d was independent of the type of impurity in Al and had the value ΔS_d = (2.2 ± 0.2) T x 10⁻⁸ V/K.

In 1972, Averback and Wagner (Ref. 18) showed that this value for ΔS_d was larger than expected in the absence of electron-phonon

mass enhancement. However, their calculation was limited by several approximations and uncertainties.

In 1975, Douglas and Fletcher (Ref. 19) measured the NE coefficients for Cd and W. Because the Debye temperature of Cd is low (~200K) the phonon-drag component of ϵ " yx did not vary as T³ over the temperature range they studied, and since the diffusion part is separated from the phonon-drag component by extrapolation to T = OK, the uncertainty in their data did not able them to reach any conclusion concerning enhancement. For W, their data did not agree with Long's (Ref 15) and again the temperature dependence of the phonon-drag component did not vary as T³ so that, again, no clear conclusion concerning any enhancement could be drawn.

In March 1976, Opsal et al (Ref. 6)--for experimental and theoretical details see Refs. 20 and 21--for the first time demonstrated the presence of mass-enhancement using measurements of ΔS_d for a dilute AlGa alloy. Ga was chosen because it had been shown (Ref. 22) to be the nearly isotropic scatterer in Al needed for the model of Averback and Wagner to be applicable to the experimental data. Opsal et al. also extended the Averback and Wagner calculation beyond a free-electron model, and showed that band structure corrections could not explain the too-large value of ΔS_d noted by Averback and Wagner. Having run out of ways for the experiment and the Averback and Wagner analysis to be wrong, Opsal

et al. then re-examined the question of whether mass-enhancement should be present in thermopower. They concluded that although Prange and Kadanoff (Ref 11) were correct that electron-phonon mass enhancement is not observable in electrical conductivity, they were not correct for thermopower. They showed that for elastic impurity scattering, if all of the properties of the electrons are consistently renormalized, then this renormalization cancels out of the electrical resistivity and the thermal conductivity, but does not cancel out of the diffusion component of the thermopower.

Shortly thereafter, Opsal (Ref. 4) showed that the phonon-drag components of the thermoelectric tensor are not enhanced, and that in the high-field limit, $(\varepsilon''_{yx})_g$ has the same $\frac{1}{B}$ variation with magnetic field as does $(\varepsilon''_{yx})_d$.

Although Opsal et al (Ref.6) had demonstrated both theoretically and experimentally the presence of electron-phonon mass enhancement in thermopower, the accuracy with which they could determinine the size of this enhancement was limited. The presence of both giant Quantum Oscillations (Ref.8) and small additional terms in the thermopower (Ref.6) make it unlikely that further measurements of ΔS_d for Al or any other metal would allow a more accurate determination of the enhancement. On the other hand, Nernst-Ettingshausen (NE) coefficient measurements have two advantages over thermopower measurements

- i) In the high field limit ϵ " $_{yx}$ can be extracted directly from the NE coefficient, because it has the simple form of equation (1.14)
- ii) Giant quantum oscillations do not seem to be as large in the NE coefficient as in the thermopower.

In 1976, Fletcher (Ref. 22) measured the NE coefficient of a single crystal of Molybdenum and found the expected temperature dependence of the electron-diffusion and phonon-drag components. From the data, he found Y^t to be within 6% of Y^c and with this uncertainty he came out with the expected enhancement of $\lambda = 0.3$ with uncertainty of 25%.

In May 1977, Thaler et al (Ref. 3) measured the high-field Nernst-Ettingshausen coefficient of polycrystalline Al from 1.8K to 5K, and separated the coefficient into electron-diffusion and phonon-drag components as described earlier. From the diffusion component of the NE coefficient they found the transport heat capacity Y^t to be identical to the experimental electronic heat capacity Y^c for Al, within a probable uncertainty of 3%. From the approximate value of λ_0 = 0.45 for Al, this leads to a probable uncertainty of about 10% in the magnitude of many-body enhancement λ_0 . The experimental difficulty in measuring P^a in an uncompensated

metal is the smallness of the NE voltage. Their Al sample, which was 0.25mm thick, produced only 5nV for 10mW of heat and a 2T magnetic field. A plot of their data $\frac{P^a}{R}$ as a function of magnetic field B for two different temperatures is shown in figure (1.1). At both temperatures, $\frac{P^a}{R}$ is independent of field above 0.8T. Figure (1.2.a) shows $\frac{P^a}{B}$ plotted against T^2 , which is expected to be a straight line in the absence of Umklapp scattering, with an intercept at T=OK of $\frac{P_d^a}{B}$ (The diffusion component of NE). Since this plot was not exactly a straight line, they also plotted $\frac{P^a}{B}$ against T³. which gave an apparent straight line [Figure 1.2.b] that had no specific theoretical justification. As shown in Figures (1.2.a) and (1.2.b) the extrapolation of these two plots led to values for $\frac{p^a}{p}$ which differed by less then 0.5% from each other. Their best value for $\frac{P^a}{D}$ is 5.88 x 10⁻¹¹ m³ j⁻¹ with an uncertainty of 2%. This value was compared with an expected value of $\frac{\gamma^c}{L_a(n_a-n_b)^2e^2} = 5.90 \text{ x}$ 10^{-11} m 3 j $^{-1}$ calculated from the accepted electronic heat capacity γ^c of 1.360 mj mol⁻¹ K⁻² Dixon et al (Ref. 7) and the Aluminum

lattice parameter of 4.032A° Pearson (Ref. 23) The uncertainty in γ^c was less than 1% and the ratio $\frac{\gamma^\tau}{\gamma^c}$ from their measurement came out to be 1.00 \pm 0.034.

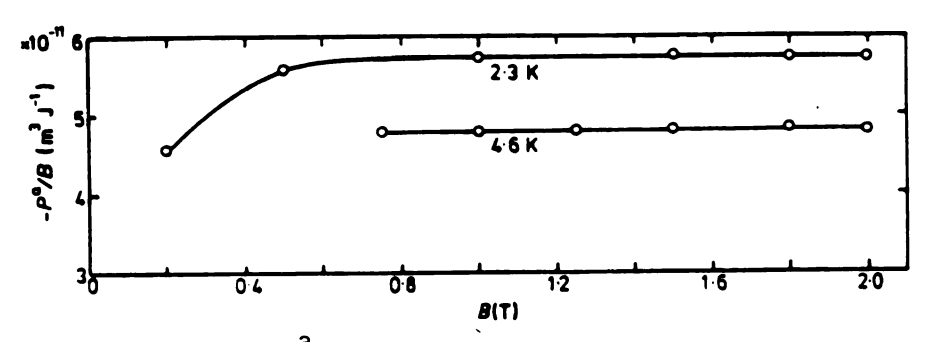


Figure (1.1) $\frac{P^a}{B}$ as a Function of Magnetic Field B for Temperatures 2.3K and 4.6K.

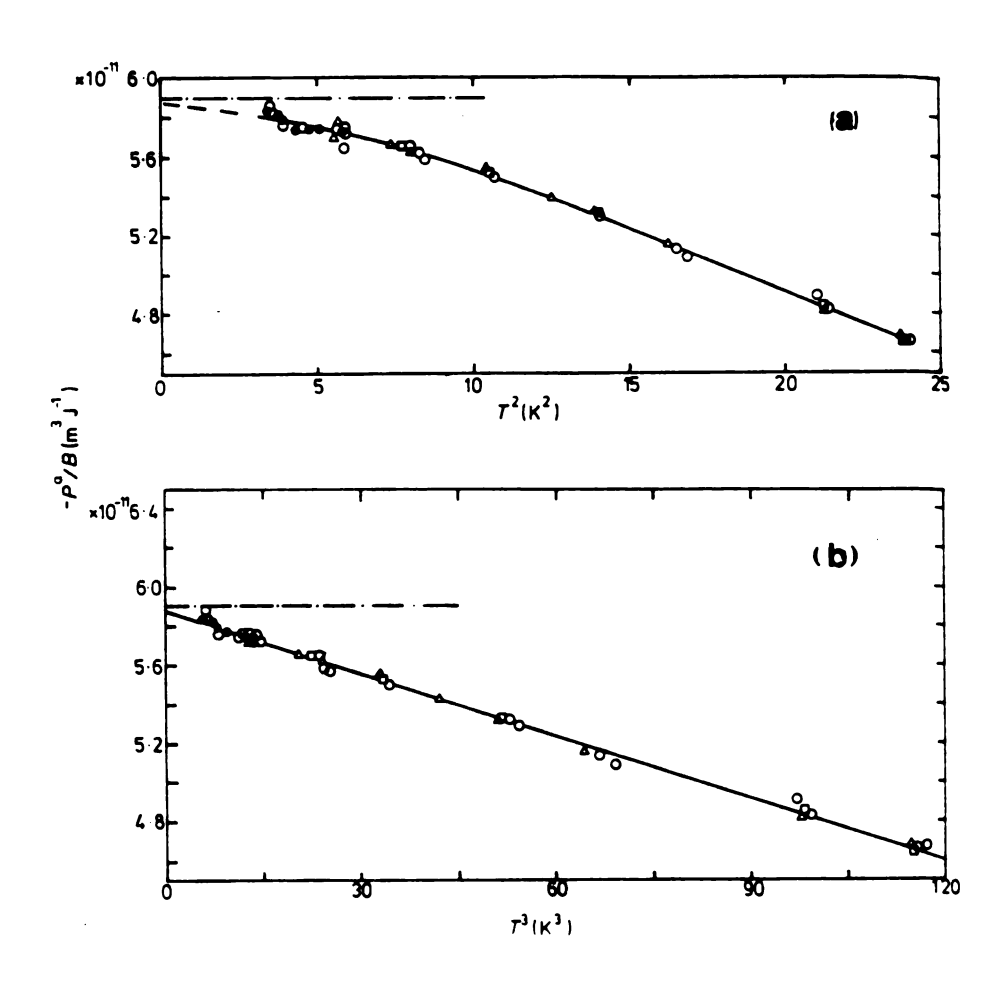


Figure $(1.2.a,b)\frac{P^a}{B}$ as a Function of T^2 (a) and T^3 (b) for Magnetic Fields of 1.5 $T(\Delta)$, 1.8 $T(\Box)$, 2.0 T(o) and 2.1 $T(\bullet)$. The broken lines indicate the value predicted from the electronic specific heat Υ^c , which contains the enhancement factor $(1 + \lambda)$.

In 1977, Lyo S.K. (Ref. 24) studied the enhancement of the electron diffusion thermopower microscopically, and found that the thermopower is enhanced not only by the mass enhancement, but also by an additional electron-phonon modification of the quasiparticle velocity. In a model of weak s-wave scatterers this mechanism added an additional term $\lambda/2$, so that the total enhancement was predicted to be 1 + 3/2 λ .

In May 1978 Vilenkin and Taylor (Ref. 25) found additional corrections to the thermopower which, for the case of weak s-wave scattering, increased the total enhancement of the thermopower to 1 \pm 2 λ .

A few months later in November 1978. Vilenkin and Taylor (Ref. 26) extended weak s-wave calculations still further, and found that the electron-phonon renormalization of the impurity scattering corrections to the low-temperature Seebeck coefficient of dilute alloys almost completely cancel corrections due to the electron-phonon renormalization of the electron energy, velocity, and relaxation time. They argued that "For normal valences the electron-phonon corrections are reduced by a partial cancellation to a few percent of some recently predicted values".

In January 1980, Ono and Taylor (Ref. 27) investigated the Seebeck coefficient in dilute alloys at low temperature using a more realistic model than the weak s-wave model previously considered. They assumed that free electrons are scattered by a random array of

fixed impurities and interact with longitudinal Debye phonons through a Fröhlich Hamiltonian. They found that for a screened Columb potential, the net electron-phonon enhancement of the Seebeck coefficient is close to the mass-enhancement factor $1 + \lambda$ suggested by Opsal et al (Ref. 6).

In August 1980, Ono (Ref. 28) added two more impurity potentials to the previous investigation by Ono and Taylor (Ref. 27): i) The screened Coulomb potential with Friedel's extension (Ref. 29) of the Thomas-Fermi approximation; and ii) The square-well potential. He found that the electron-phonon enhancement of the Seeback coefficient again generally came out numerically close to the mass-enhancement factor $1+\lambda$.

In 1982, Rammer and Smith (Ref. 30) noted that since 1964 the electron-phonon mass enhancement had been obtained only for free electron models and Debye-phonons with simple model impurity potentials. But they argued that for calculating thermoelectric properties even in the absence of renormalization, the free electron models are not adequate. They focussed on the high-field limit

$$\omega_{c} \cdot \tau \gg 1$$
 (1.22)

where ω_c is the cyclotron frequency and τ is the collision time. To simplifying the problem, they neglected the effect of impurity and phonon scattering. To treat the effect of renormalization they

used the Keldysh method (Ref. 31). Their calculation gave a renormalization factor of

$$m^* = m (1 + \lambda - c\alpha\lambda) \tag{1.32}$$

where c is an energy-independent constant that is 1/2 for free electrons interacting with Debye-phonons and α is:

$$\alpha = \frac{\int_{0}^{E_{F}} g(E) dE}{g(E_{F}) \cdot E_{F}}$$
 (1.33)

Here $g(\epsilon)$ is the electronic density of states. For $g(\epsilon) \sim \epsilon^{1/2}$ as in case of free electrons, $\alpha = 2/3$. This investigation yields an overall reduction in the electron-phonon enhancement factor from (1 + λ) to (1 + $\frac{2}{3}$ λ).

In February 1983, Hänsch and Mahan (Ref. 32) continued their previous work on the derivation of new transport equation for many-particle systems in dc electric fields (Ref. 33). They derived the transport equation by both the Keldysh (Ref. 31) and the Kadanoff (Ref. 11) methods for nonequilibrium formulation of many-body systems, and calculated the low-temperature thermopower in high magnetic field. They essentially confirmed the statement made by Opsal, Thaler, and Bass that electron-phonon mass enhancement is

șres

...

...

tra 2.

:::

76

...

()

;

S:

•

,

present in the adiabatic thermopower in high magnetic field and that this enhancement is $(1 + \lambda)$.

(1.3)PRESENT THESIS:

As noted in the introduction, this dissertation has two parts:

1. Construction of a general purpose system for measuring high-field transport coefficients using a SQUID at ultra-low temperature; and

2. Use of this system for measuring the off-diagonal diffusion component of the thermoelectric coefficient of Al below 1K. As also noted, this coefficient is expected to be subject to many body renormalization involving the electron-phonon mass enhancement.

(1.3.1) The Construction Problem:

The main construction problem involved vibration isolation in a dilution refrigerator. To illustrate the problem, we use a simple example.

In the presence of a magnetic field, one of the most intensive sources of noise is due to mechanical vibration of the sample leads. With the refrigeration capacity of our refrigerator, a sample of thickness a few tenths of a mm, and a magnetic field of 10 kG (1 T), we would expect a Nernst-Ettingshausen voltage across the sample of about 10⁻¹¹V. Assume that the voltage leads and the sample make a loop which has an effective change in area of 1 mm² per vibration

and which vibrates with a mechanical frequency of 10 Hz. Then the noise voltage generated in the loop would be

$$V_{N} = \frac{d(B \cdot A)}{dt} = 2\pi f B A Cos (2\pi f t). \qquad (2.1)$$

With the above assumptions, $V_N \sim 6 \times 10^{-5}$ volts, about 6×10^6 times bigger than the assumed signal. This model illustrates the importance of vibration isolation of the cryostat, and explains the need for the multiple-stage vibration isolation described in Chapt. II.

Thermometry in high magnetic field at low temperature was another important subject in this study. For Righi-Leduc coefficient measurements, transverse temperature differences had to be measured very precisely, and part of this dissertation was to make and calibrate thermometers with high resolution at very low temperature in the presence of high magnetic field. The construction techniques and calibration of the thermometers are also described in Chapt. II.

(1.3.2) Thermoelectric Measurements on Aluminum:

For the following reasons we chose an Al foil for our experiments.

- 1. The most accurate measurements of ϵ " are possible on uncompensated metals like Al, as noted above.
 - 2. Al has a large electron-phonon mass enhancement, $\lambda \sim 0.45$.
- 3. Al has a simple, well understood electronic structure with a nearly spherical Fermi surface, and its Debye temperature is sufficiently high (about 430K) so that phonon-drag effects are manageably small. It is not reactive, so that it is easy to work with.
- 4. Previous measurements on Al extended down to only 1.8K. It is therefore of interest to go to lower temperatures to reduce uncertainties of extrapolation and to make sure that no unexpected behavior occurs. In this thesis, we extended measurements down to a refrigerator temperature of 0.147K. From Fig. 1.2, we see that extrapolation to T = 0K from such a low temperature, should introduce an uncertainty of much less than 1%.

As noted above, in addition to measuring the Nernst-Ettingshausen coefficient, NE, we also measured the Hall Coefficient, R_H , and the Righi-Leduc Coefficient, R_L , as cross-checks on the sample thickness and the amount of heat flowing through the middle of the thin sample. These measurements helped us to reduce the uncertainties in the quantity of ultimate interest, $\epsilon_{yx}^{"}$.

The remainder of the thesis is organized as follows:

Chapter II provides a description of the experimental techniques.

Chapter III provides the theoretical background for the calculation of the high field limits of the Nernst-Ettingshausen (NE), Hall ($R_{\rm H}$) and Righi-Leduc ($R_{\rm L}$) coefficients.

Chapter IV furnishes the experimental data and our conclusions about the low temperature, high magnetic field NE, $\rm R_{H}, \, R_{L}$ coefficients of Al.

CHAPTER II

EXPERIMENTAL TECHNIQUE

(2.1)Introduction:

Since the dilution refrigerator, current comparator, SQUID, and other pieces of equipment have already been described elsewhere (Ref. 35, 36), in this chapter only some modifications are described in detail.

After brief remarks concerning the refrigerator, bridge, and the SQUID, different techniques for vibration isolation of the system are described, especially the centering device. Then the low temperature high magnetic field thermometry is briefly reviewed, and the thermometer preparation techniques and calibration are discussed. Sample preparation and the sample contact techniques are next. The superconducting magnet and its connections to the cryostat are described. Finally, the reference resistor is discussed, and the method of using the SQUID in a feedback loop is described.

(2.2)Dilution Refrigerator:

To obtain temperatures on the order of .1K continuously, a locally built dilution refrigerator was used. The details of this dilution refrigerator are described in Chi-Wai Lee's dissertation (Ref. 36). The refrigerator was capable of giving temperatures ranging from 4.2K to 60mK. First the system was cooled down to

•

exc)*

2.

163

.

\$43 \$41

ie:

1.5

• •

•

14

liquid nitrogen temperature (~77.4K) in about 12 hours using He exchange gas. Further cooling to liquid helium temperature (4.2K) was done by transferring liquid helium into the inner dewar (Figure 2.1). Cooling to 1.3K was obtained by pumping on the liquid helium in a 1K pot. From this temperature the dilution refrigerator reached the lowest temperature (~60mK at the mixing chamber) after a few hours of circulation of the 3He/4He mixture.

The power of the dilution refrigerator at very low temperatures was very important, because for NE measurements a thermal current is sent through the sample and the refrigerator must be able to absorb this heat at the temperature of interest. As the temperature decreases, the cooling power of the dilution refrigerator decreases also. At 150mK the cooling power of the dilution refrigerator is 100 µWatts; at 100mK, the power 40 µWatts. At the lowest temperature (60 mK), the cooling power drops to zero. As discussed below, the cooling power of the refrigerator plays an important role in determination of the sample thickness and the lowest temperature at which accurate NE measurements can be made.

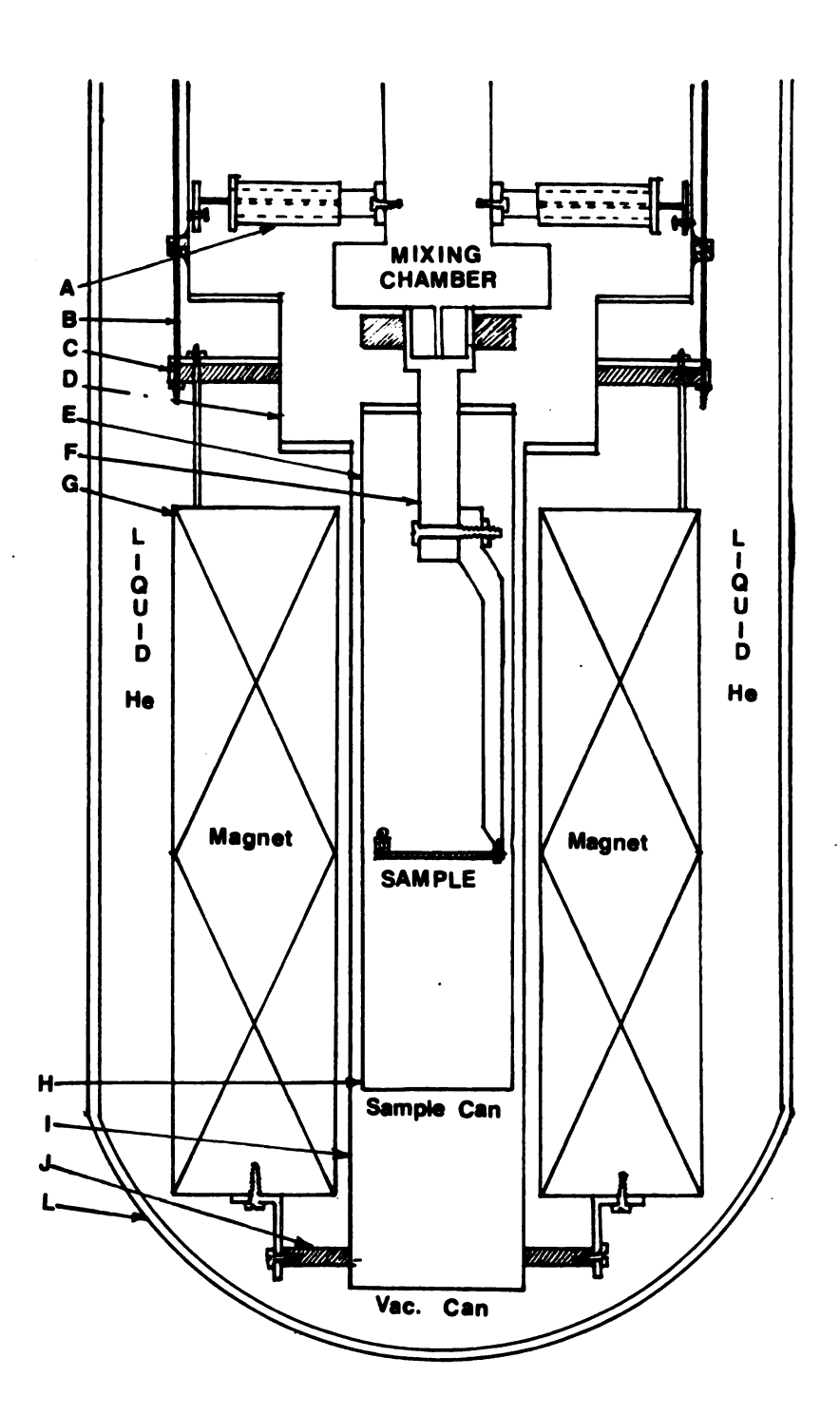


Figure (2.1)Diagram of the Sample, inside the superconducting Magnet, with the connections between the mixing chamber and the vacuum can through the centering device.

- A Centering Device.
- B Magnet Support.
- C Teflon rings for attachment of the magnet to the vacuum can.
- D Vacuum Can.
- E Sample Can.
- F Sample Support.
- G Magnet.
- H Sample Can.
- I Vacuum Can.
- J Teflon rings for attachment of the magnet to the vacuum.
- L Liquid He Dewar.
- M Teflon ring for attachment of the sample can to the mixing chamber.

Figure (2.1)Diagram of the Sample, inside the superconducting Magnet, with the connections between the mixing chamber and the vacuum can through the centering device.

(2.3) High Precision (0.1 PPM) Resistance Bridge:

The resistance bridge consisted of a commercial direct current comparator (Ref. 37) and a SQUID (Superconducting Quantum Interference Device) (Ref. 36) which was used as a sensitive null-detector. The current comparator could read the ratio of two currents (Slave and Master) with a precision of better than 0.1 PPM using a set of eight decade-dials and the technique of averaging beyond the last dial.

(2.4)SQUID:

The SQUID was used as a high precision null-detector. It provides a very high current sensitivity, limited only by the thermal Johnson (voltage) noise in the SQUID circuit resistance R:

Johnson Noise =
$$\sqrt{4k_BTR\Delta f}$$
 (2.1)

where k_B is the Boltzmann constant and Δf is the band width. The basic principle of the SQUID is based on the Josephson effect (Ref. 1). The SQUID used in our system was a symmetric point contact r.f. biased device purchased from SHE Corp. (SHE Model RMPC with SHE Model 330 electronics).

:

:-

:

ŗ

::

(2.5) Vibration Isolation of the Cryostat:

The first level of vibration isolation of the cryostat was made by using flexible bellows on pumping lines and an air mount for the cryostat. These are described in the thesis of Chi Wai Lee (Ref. 36). In addition, for standard measurements a μ metal shield was wrapped around the whole cryostat to isolate it from the earths magnetic field which is ~0.5 G.

In this study, where a magnetic field of 10-20 kG was to be applied, the noise due to vibration in the magnetic field could be very large, as explained in the Introduction. Therefore the vibration of the system had to be minimized. This was done by reducing the relative vibration of the sample with respect to the superconducting magnet in two steps. First, the magnet was rigidly attached to the vacuum can by two flanges at the ends of the magnet as described in the next section. Second, a centering device was used to produce a strong mechanical coupling between the sample and the vacuum can (Figure 2.1), together with poor thermal conduction.

(2.5.1) Magnet Supports:

The superconducting magnet was attached to the top of the vacuum can by three long 1/4" threaded brass bars, located inside the Helium bath. The magnet was rigidly attached to the vacuum can by two teflon rings, Figure (2.1). At room temperature the vacuum can had enough clearance to fit into the teflon rings, but as the

:3

cryostat was cooled down, the teflon flanges shrank and caused the magnet to be rigidly attached to the vacuum can.

Since there should be no weight hanging on the vacuum can, the magnet support bars were made out of brass, such that in the process of cooling down the cryostat, the higher thermal contraction of the brass bars relative to the vacuum can (the top part of the vacuum can was made of stainless steel), causing the magnet to push up on the vacuum can. This pressure on the vacuum can was helpful in order to keep its connections leak tight.

(2.5.2)Centering Device:

Minimizing mechanical vibration, while providing accurate centering with very low heat loss, is done by clamping the mixing chamber of the dilution refrigerator into the surrounding 4.2K vacuum can with a reentrant spider (Ref. 39) as shown in Figure (2.2).

The thermal isolation of the system was done in two different stages. A 1" x 1/16" copper band was located between the center clamp (on the top of the mixing chamber) and the external brass cylinder. This copper band was located between the two stages of thermal isolation Figure (2.3) and was thermally lagged to the continuous heat exchanger, which operated around 1.2K. The thermal isolation between the stages was provided by using Vespel (Sp-22),

purchased from DuPont. Vespel has a very low thermal conductivity.

The heat flow was calculated by the general expression:

$$\dot{Q} = -K (T) A (\frac{\partial T}{\partial X})$$
 (2.2)

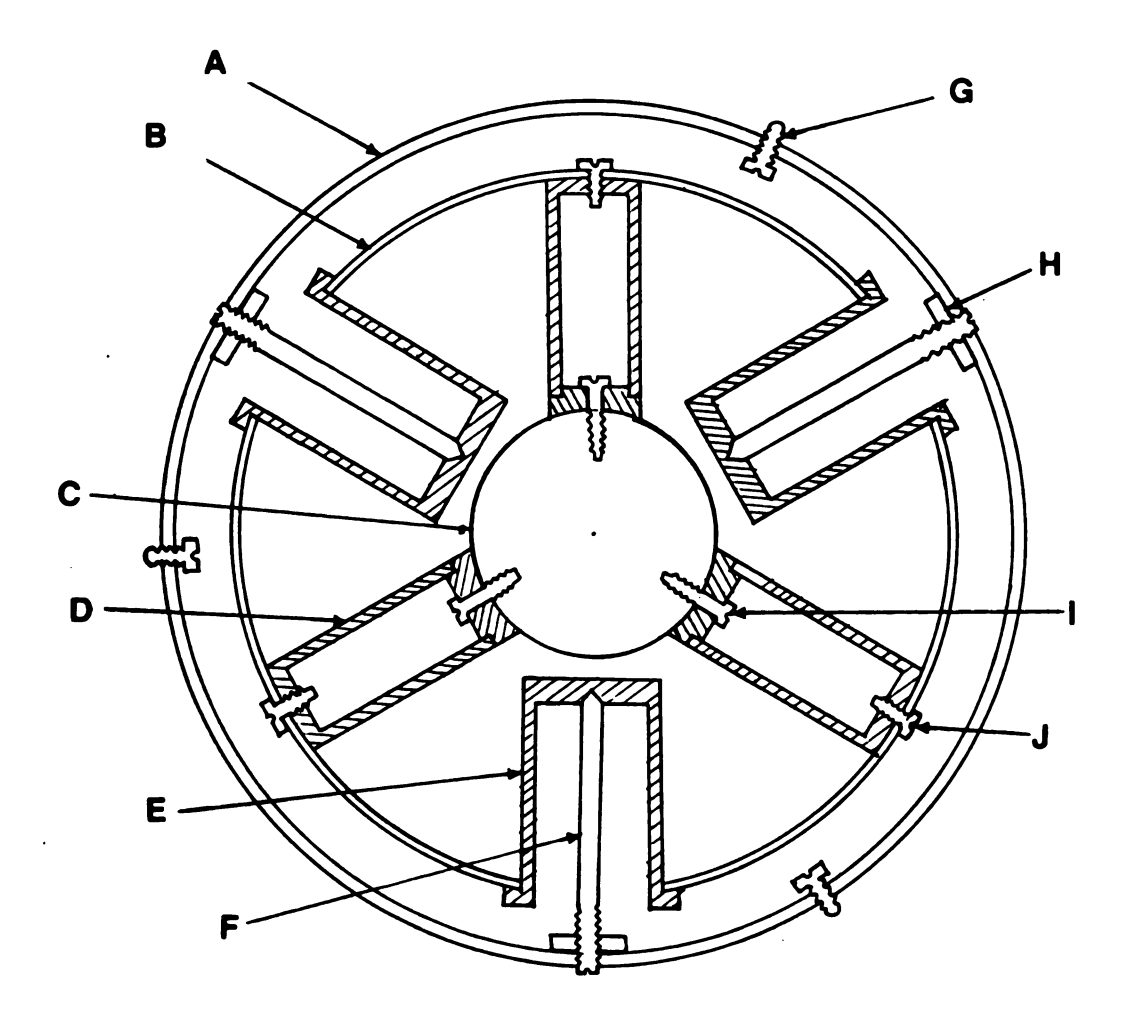


Figure (2.2)Cross section view of the centering device. A-Brass Band. B-Copper Band Heat Exchanger. C-The Upper Side of the Mixing Chamber. D-Vespel Cylinder (stage 1 of the thermal isolation). E-Vespel Cylinder (stage 2 of the thermal isolation). F-Stainless Steel Rod. G-Adjusting Screw. H-Locking Nut. I,J-Attaching Screws.

where K(T) is the thermal conductivity, and A is the average cross section of the media where $\frac{\partial T}{\partial X}$ is measured. If K (T) ~ T^n , and the heat influx is at the ends only, then the above equation may be simplified over the temperature range studied to:

$$\dot{Q} = \frac{A}{1} [K(T_h)/(n+1)] T_h$$
 (2.3)

 T_h is the temperature of the heat path at the hot end, 1 is the length of the heat path, and n is a constant which depends on the material. Equation (2.3) was used to estimate the heat flows in the system which is described next.

a)Stage 1. The thermal isolation between the mixing chamber and the 1.2K copper band heat exchanger:

Three Vespel tubes were attached to the copper band (1.2K) from one end and fitted on to the three Vespel studs from the other end. The three Vespel studs were fixed on the mixing chamber clamp by three brass screws. The thickness of the Vespel tubes in this heat path was first estimated using Equation (2.3), and then corrected experimentally so that the noise of the vibration of the system was low enough to provide good voltage sensitivity for NE measurements. Using equation (2,3) where $T_h = 1.2$, $T_c = 0.1$ K, $K = 24~\mu W~K^{-1} cm^{-1}$, the tube radius R = 1/4", the tube thickness $\Delta R = 1/16$ ", the length of the tube l = 1" and for Vespel n - 2. gives, $\dot{Q}(1) \sim 6~\mu$ Watts. This is low enough to allow temperatures below 0.1K to be reached.

b)Stage 2, The thermal isolation between the copper band (1.2K heat exchanger) and the surrounding vacuum can (4.2K):

Three Vespel tubes were inserted into the 3/8" holes on the copper band as shown on Figure (2.2). Then three 6-32 stainless steel screws were fitted inside the Vespel tubes so that they could be adjusted for centering the mixing chamber. For this adjustment three holes on the copper band provided access to the screws and their locking nuts. To fix the brass cylinder to the surrounding vacuum can, three screws with spherical shaped ends were attached to the brass cylinder. These screws could be tightened from inside by removing the lower part of the vacuum can. To allow access to the centering device from inside, the vacuum can was made out of two pieces. These two pieces were attached together just underneath the centering device.

(2.6) Thermometry in High Magnetic Fields at Low Temperatures:

Thermometry, even at zero field, becomes increasingly difficult at lower temperatures due to poor thermal conductivity of materials, thermal boundary resistance, subsequent long thermal relaxation times, and thermal gradients. The application of high magnetic fields adds to the complication because of the magnetic field dependence of the thermometers. In this thesis, high precision

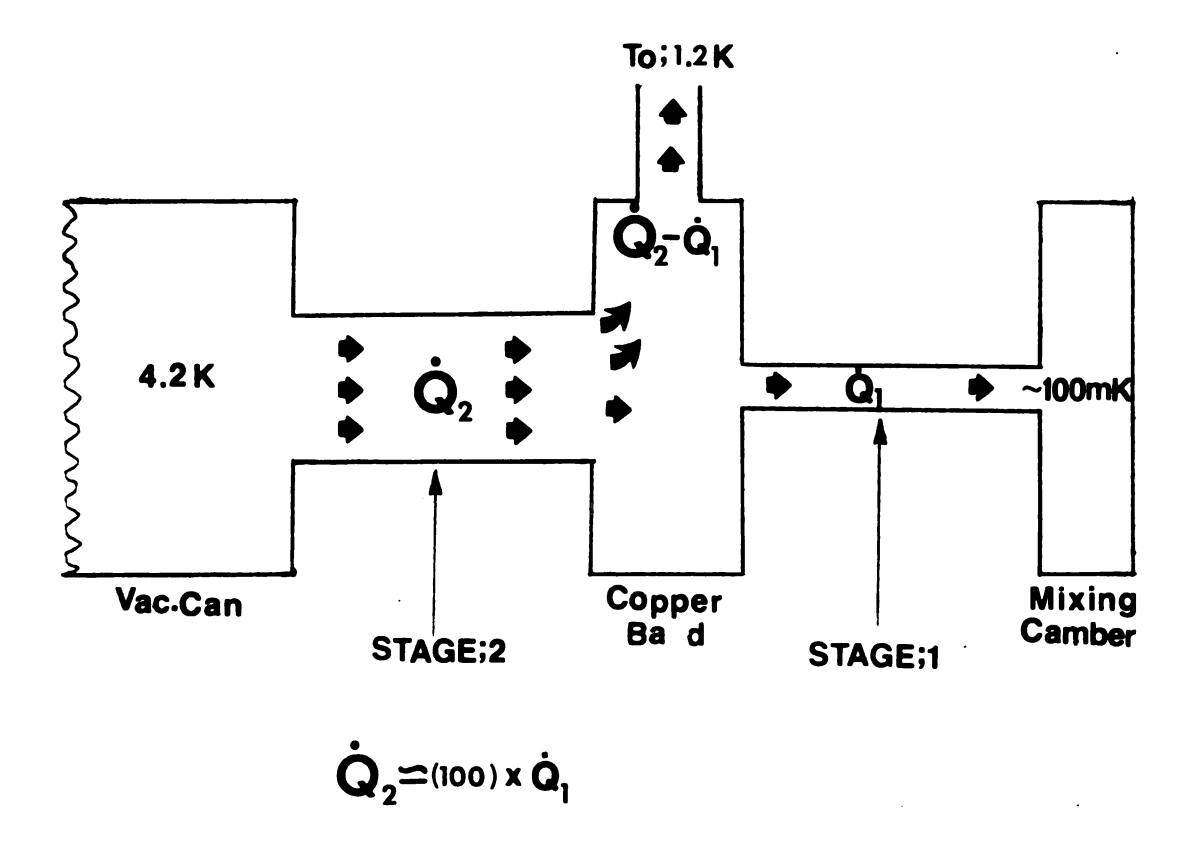


Figure (2.3)Block diagram of the two stages of thermal isolation of the centering device. Stage 1-The thermal isolation between the mixing chamber and the copper band connected to the 1.2K heat exchanger. Stage 2-The thermal insulation between the copper band and the surrounding vacuum can.

:

•÷

• •

::

•

::

1

thermometry below 1K in the presence of high magnetic fields was reviewed and different kinds of thermometers such as capacitive thermometers, germanium, carbon and Speer carbon resistance thermometers were studied. Finally the Speer carbon resistance thermometers were chosen, calibrated in the presence of the magnetic field, and used for thermometry at low temperatures and high magnetic field.

In this section, different kinds of thermometers are briefly reviewed, and then the Speer carbon thermometers are described in detail.

(2.6.1) Different Thermometers:

Capacitive thermometers are useful as transfer standards where magnetocapacitive effects are not a problem (Ref. 40, 41). But, for the following reasons they were not suitable for thermometry in this study. i)-their capacitance drifts slowly with time and occasionally shifts in value from run to run. ii)-the insensitive region of these capacitors is between 1K and 0.1K. (Ref. 42).

Germanium resistance thermometers are very sensitive and stable thermometers for a wide range of temperatures, especially for temperatures below 1K. These thermometers are typically reproducable to better than .0005K at liquid Helium temperature when cycled to room temperature (Ref. 43). But, the problem of using germanium thermometers in our study was their magnetic field dependence.

Since in this study the thermometry is in the presence of a high magnetic field, the magnetic dependence of these thermometers was a fundamental problem. Different techniques for shielding these thermometers from the magnetic field were studied such as, (A)-superconductive shields and (B)-placing the thermometers out of the magnetic field with a thermal line connection to the sample. In technique (A), because of the non-uniform magnetic field produced by the magnetic shields around the sample and in technique (B), because of the large heat capacity of the thermal line which causes a very large time constant for thermal equilibrium, neither technique was practical for the primary thermometers. But the above techniques were used for thermometer calibration as described below.

Carbon (Ref. 44, 45), carbon-glass composition (Ref 46), and Allen-Bradley (Ref 47) resistors are often used as thermometers in high magnetic fields above 1K. But these resistors are not suitable for thermometry below 1K (for Allen-Bradley below .5K), because of their very high resistances at lower temperatures.

Speer Carbon resistors (Ref. 48, 49) were found to be the most appropriate sensors to be used as low temperature high magnetic field thermometers in this study. Matsushita carbon resistance thermometers (Ref. 50, 51) also seemed potentially suitable as thermometers. But, we could not find information, either in the U.S. or Japan, about the manufacturing company. Thus, Speer resistors were used as our thermometers. Speer resistors at zero

•1.

magnetic field have a temperature dependence in the form of (Ref. 49)

$$R = R_o \exp (AT^{-1/4}) = R_o \exp (AB^{1/4})$$
 (2.4)

where R_o and A are constants and B = $\frac{1}{T}$.

The magnetic field dependence of the Speer resistors is defined as: $\frac{\Delta R}{R} = [R(T,H) - R(T,0)]/R(T,0)$. In Ref. 49, it is shown that $\frac{\Delta R}{R}$ is a linear function of log (H/T), i.e.:

$$\left|\frac{\Delta R}{R}\right| \sim \log(H/T)$$
 (2.5)

where the magnetoresistance is negative (i.e., application of a field decreases R at fixed temperature). From Equation 2.5, we see that each factor of 2 increase in H/T increments $\frac{\Delta R}{R}$ by a fixed amount. For example,

 $|\Delta R/R| = 4\%$ at H/T = 20 kG/K (H = 20 kG, T = 1K). $|\frac{\delta R}{R}|$ increases to 8% at $\frac{H}{T} = 40$ kG/K (H = 40 kG, T = 1K or H = 20KG T = .5K or), and $\frac{\Delta R}{R}$ increases to 12% at $\frac{H}{T} = 80$ kG/K (H = 20kg, T = ,.25K or H = 80Kg, T = 1K or).

(2.6.2) Thermometer Preparation:

The thermometers were made from Speer carbon resistors which were purchased from the Speer carbon company. W.C. Black et al

(Ref. 48) found, that Speer resistors of grade 1002 in various nominal resistance values from 100 - 500 Ω are the most suitable for very low temperature work. For this reason all of our thermometers were made from 100 Ω 1/4 W speer carbon resistors.

First the Speer resistors were cut in forms of discs with heights of about 3mm. Then one side of the discs were flattend so that the graphite appeared, Figure (2.4). (This is the side of the thermometer which sits on the sample, and it was made flat for better thermal connection with the sample.) Then the flat side was covered with cigarette paper which was soaked in GE 7031 varnish. The thermometer leads were superconducting NbTi (0.004" diam) wires which were attached to the two sides of the Speer disk with silver paint. After a few hours, when the silver paint was completely dry, the thermometers were baked at 200°C for about ten hours. The temperature and the time of baking complete the diffusion process of the silver paint into the Speer. (If the diffusion of the silver paint into the Speer is not complete, the resistance of the Speer thermometer changes as a function of time from run to run. In such a case the time or the temperature of baking must be increased).

After baking, the thermometers were painted with Duco cement and then a little silicon glue was used on the leads at the thermometer ends to provide strength with flexibility. The leads

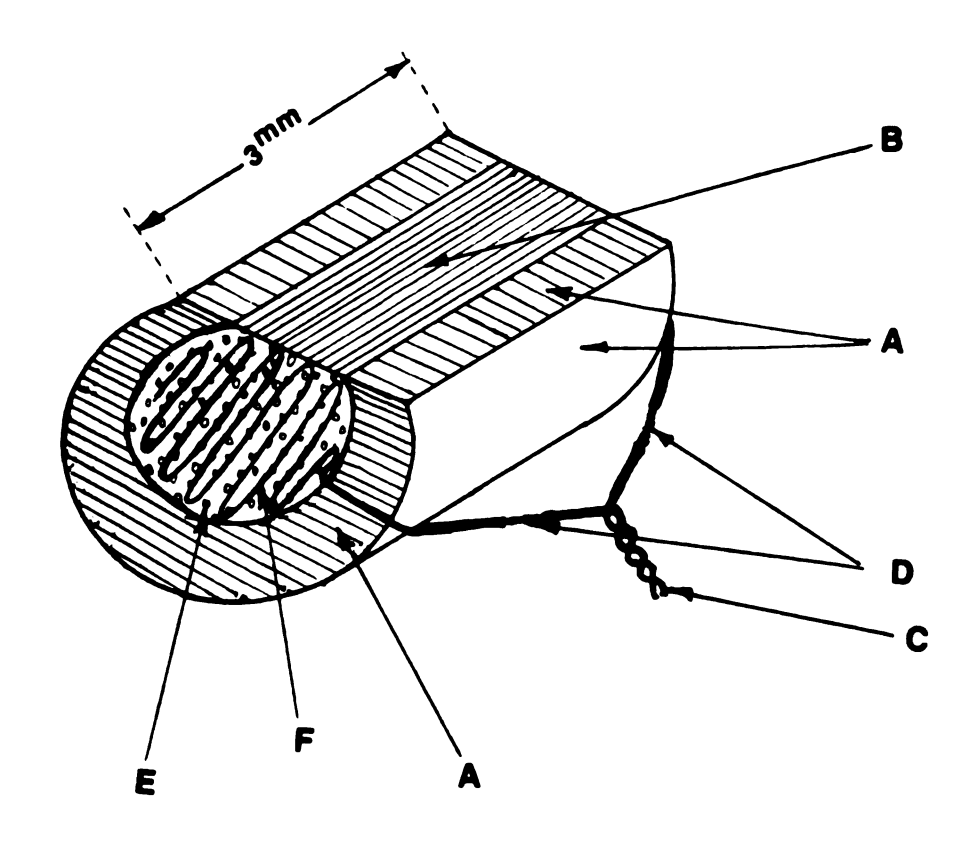


Figure (2.4)Speer Carbon Thermometer: A-Speer Carbon Resistor Body. B-Speer Graphite. C-Superconducting NbTi Leads. D-Copper Clad is removed from the superconducting wire. E-Silver paint for electrical contacts between the leads and the speer carbon thermometer. F-Superconducting wire with the electrical isolation removed from it.

were twisted together exactly the same way as the sample leads, and then were wetted with Apiezion N-Grease for better thermal conduction to the cold line.

Finally the Speer thermometers were mounted on the sample limbs with the help of a non-magnetic spring and some N-Grease (Fig 2.5), and its leads were glued to the sample support with GE 7031 varnish.

As is shown in Figure (2.4), the superconducting wires have a copper clad. This copper clad was etched away over a short length (-3mm), for better thermal isolation of the thermometers from the environment. Overall, about ten thermometers were made using this technique. Four of these were used for measuring the transverse and the longitudinal temperature gradients. These thermometers, designated T_{right} , T_{left} , T_{hot} , T_{cold} were mounted on the sample limbs. Two other themometers, used for calibrating the above four thermometers, were thermally connected together with an annealed pure polycrystalline silver wire. One of the calibration thermometers was mounted underneath the sample (in the magnetic field), while the other was mounted out of the magnetic field, by the mixing chamber. The Speer thermometer connected to the mixing chamber with a NbTi box.

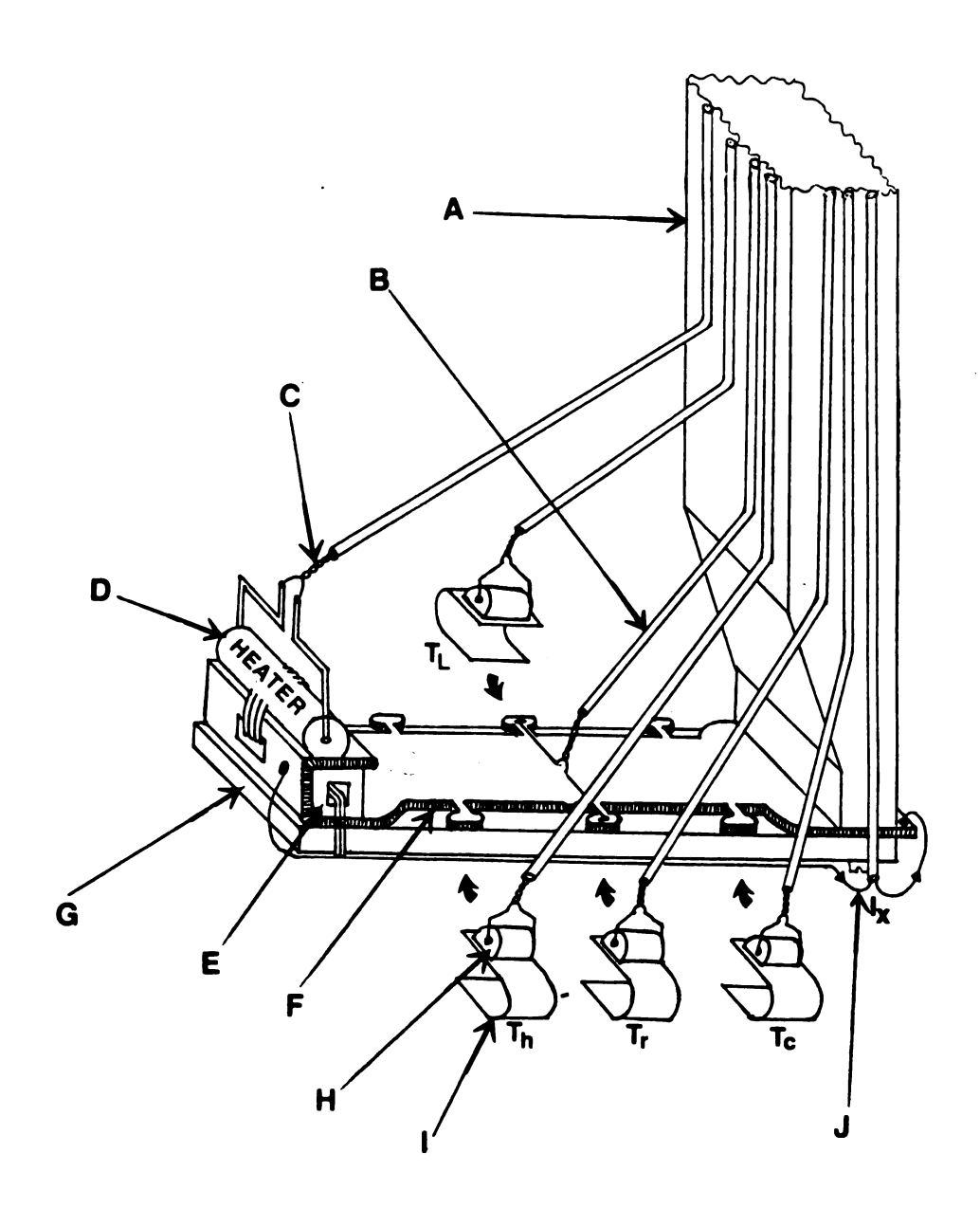


Figure (2.5)Sample Holder: A-Maine copper support. B-Pb shield for sample voltage wires. C-Heater leads. D-Heater. E-Heater stand. F-Aluminum sample. G-Vespel substrate. H-Thermometer. I- Thermometer holding-spring. J-Current leads to the sample.

(2.6.3) Thermometer Calibration:

A germanium resistance thermometer, called GRT_2 , was used as a reference thermometer for calibration of the Speer thermometers. GRT_2 itself was calibrated in three steps. The details of the three step calibration are given in the Ph.D. thesis of Z.Z. Yu (Ref. 35).

GRT₂ was mounted by the mixing chamber, inside a Niobium box which isolated GRT₂ from the magnetic field. GRT₂ was thermally anchored to the two Speer calibration thermometers, and the calibration in the magnetic field was done in two stages as follows:

First the Speer thermometer by the mixing chamber (T_{mix}) and the Speer thermometer by the sample (T_s) were calibrated against GRT2 at zero magnetic field. Then the magnetic field was turned on and T_s was calibrated against T_{mix} at different magnetic fields (T_s) is in the magnetic field, while T_{mix} is at zero field). After this calibration, T_s was our reference thermometer in the magnetic field, and all the other thermometers T_R , T_L , T_C and T_H were calibrated against T_s at different magnetic fields, Figure (2.5.b).

For rough measureurets, the magnetic field dependence of the thermometers were fitted to equation (2.5). For very accurate measurements of T_R and T_L , each thermometer was calibrated as follows for every temperature reading at a given magnetic field.

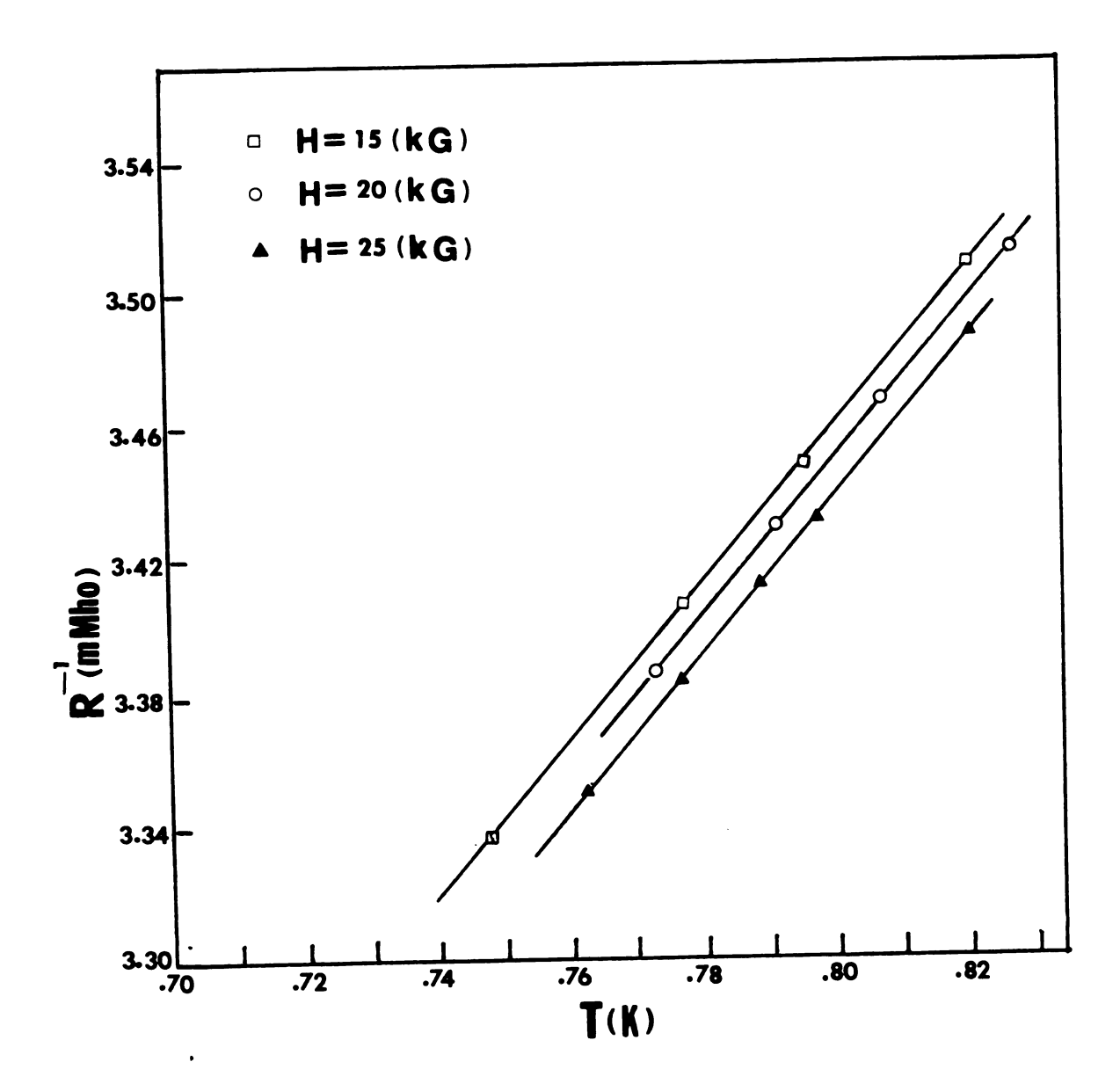


Figure (2.5.b) Admitance of Tc as a Function of Temperature in Magnetic Fields; 15, 20, 25, kG.

First, the magnetic field was ramped up to B_{O} . Then the thermal current Q_{X} was ramped up and the NE voltage (the transverse voltage) was measured. The conductances of T_{R} and T_{L} were measured with the SHE conductance bridge (Model PCB). Then for the calibration of T_{R} and T_{L} , Q_{X} was ramped down to zero while the magnetic field B was held constant. Consequently the temperature gradient (in all directions x and y of the sample) dropped to zero and,

$$T_R = T_L = T_C = T_H = T_S = T_{MIX} = GRT_2$$

For calibration of, for example T_R , some heat was sent into the mixing chamber and the temperature of the whole sample was raised along with all of the thermometers until the conductance bridge read the same value for T_R as was measured before (on R_L measurements when Q_X was flowing into the sample). Since all the thermometers were at the same temperature, T_R was calibrated directly from GRT_2 . For the calibration of T_L or T_C exactly the same technique was used, but, obviously, different amounts of heat were needed to bring each thermometer to its appropriate temperature.

(2.6.4)Temperature Regulation:

SHE model PCB conductance bridges were used to measure the conductance of the thermometers in the 4-terminal configuration with an accuracy of better than .5%. Using low excitation voltage (10 to μV), eliminated the problem of self heating. $100\mu V$ excitation

voltage could be used only at temperatures above .5K, while $10\mu V$ excitation voltage gave 1% accuracy with no self heating problems. The conductance bridges were self-balancing, so that in addition to their use in temperature measurements, their differential outputs were also used for temperature regulation(Ref.36). Because of their low noise, the bridges were ideal for use with a temperature controller to regulate the mixing chamber temperature. The temperature controller (Ref.36) had the usual differential and integral controls with adjustable time constants and proportional controls. Twelve output power levels were available for better temperature regulation at different temperature ranges. For regulating the temperature, $T_{\rm c}$ was used as the reference thermometer, and the mixing chamber heater was used for controlling the temperature. Using the conductance bridge, we could control the temperature with resolution of better than 10^{-4} K. This resolution was required for $R_{\rm L}$ measurements.

(2.7)SAMPLE

(2.7.1)Sample Size:

The length and the width of the sample were limited by the dimensions of the superconducting magnet. The magnetic field was directed along the cylindrical axis of the magnet. To measure transverse Magneto-transport effects, the field had to be perpendicular to the sample. Since the inner diameter of the magnet was about 2", the length of the sample was limited to about 1.1/2". The width of the sample was ~1/8" and the sample had six limbs, two for transverse and four for longitudinal measurements, (Fig. 2.5).

The thickness of the sample was also limited. Consider equation (1.15) where P^a has its high magnetic field limit, and $U_{\chi}=Q_{\chi}/(W.t)$. The NE transverse voltage is;

$$V_{v} = E_{v} \cdot W = P^{a} \cdot U_{x} \cdot W = \frac{P^{a} \cdot Q_{x}}{t}$$
 (2.8)

Since P^a is a constant, and the heat flow Q_x is limited by the power of the dilution refrigerator, V_y is proportional to 1/t--i.e. the thinner the sample, the larger V_y.

On the other had, having a very thin sample brings problems. These include the difficulty of precise measurement of its thickness, the problems associated with the handling a very thin foil with poor mechanical strenth, and the uncertainty in the magnitude of the heat flow density at the center of the sample due to heat flowing through the substrate.

To ensure that the NE transverse voltage V_y was at least 10^2 times the noise level in the SQUID circuit $\sim 10^{-13} V$, we needed to use a (2×10^{-3}) " thick Aluminum sample.

(2.7.2)Sample Preparation:

The Aluminum sample was purchased in form of a 1" wide and 2×10^{-3} " thick Aluminum foil from Cominco American. We measured the RRR of this pure Aluminum foil and it was;

$$RRR = \frac{\rho(300K)}{\rho(4.2K)} = 2300$$

The sample was cut with a spark cutter. The sample cutter was made out of Brass (Fig. 2.6). It had six limbs for transverse and longitudinal voltage and temperature measurements, and two wide ends for thermal and electrical current inputs.

The limbs were elliptical pads (about 1/8" x 3/64") which were connected to the sample by 1/32" wide and 1/16" long rectangular bridges (Fig. 2.6). The Aluminum foil was spark cut under paraffin oil, while it was sandwiched between two thick Aluminum plates. Without the Aluminum plates for holding the thin sample flat, the edges of the sample did not come out smooth.

(2.7.3) Annealing:

The sample was annealed at 420°C for twelve hours and the temperature was then gradually reduced to room temperature in about five hours. During the annealing process, the sample was placed between two very clean pieces of Alumina to keep the sample flat.

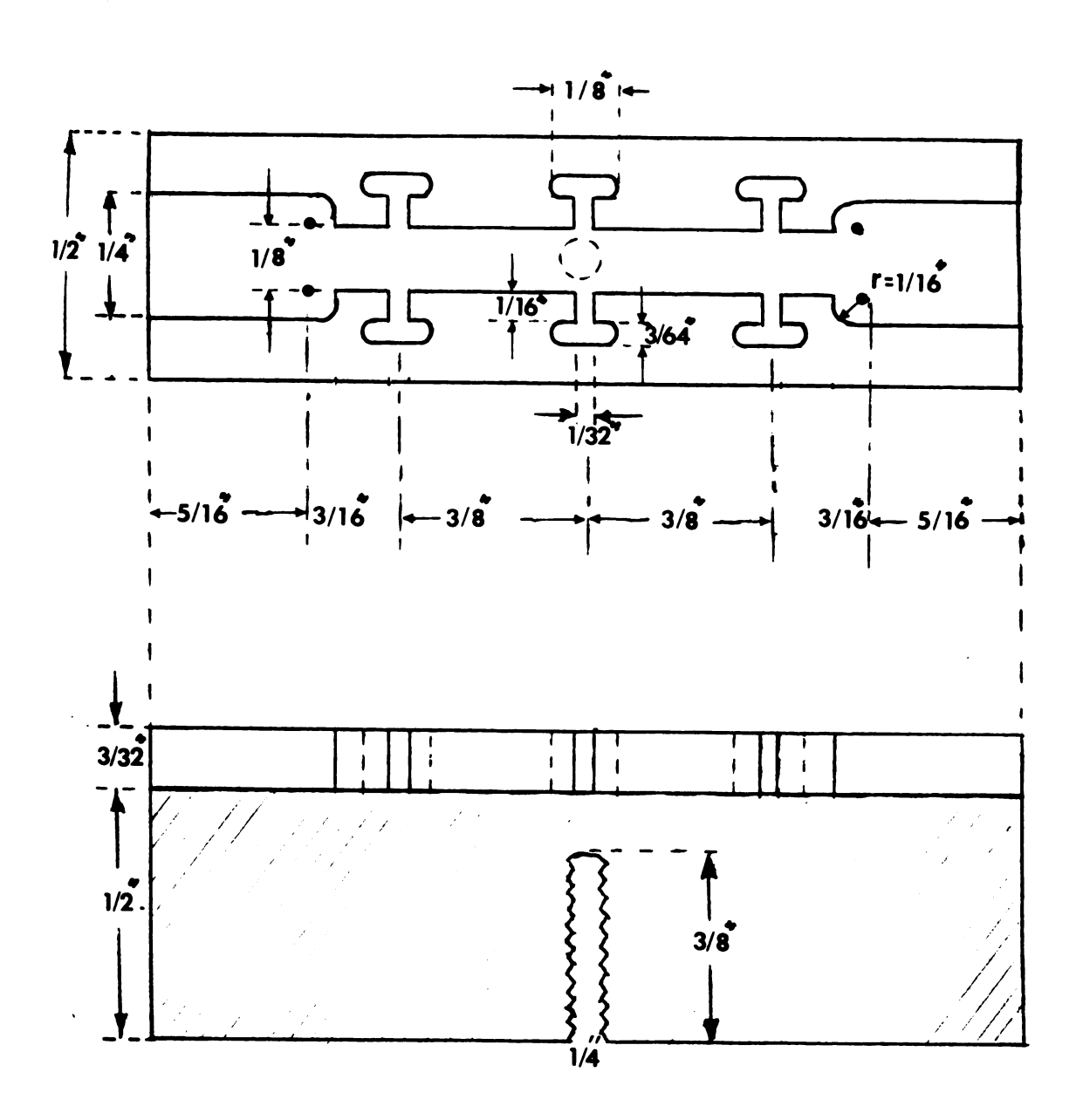


Figure (2.6)Brass sample cutter cross section.

(2.7.4)Sample Connections:

The sample was connected to the cryostat electrically, thermally, and mechanically through three independent parallel lines as follows:

a) Electrical Connection:

Three pairs of NbTi (d = 0.004") superconducting wires were connected to the sample; two for sending electrical current into the sample and four for measuring longitudinal and transverse voltages across the sample. Since the NE measurements were made through the two middle transverse leads, using the SQUID, this pair of NbTi wires was twisted together very carefully and then fed through a Pb tube to shield the wires from the magnetic field. It was essential that the electrical contacts of this pair of wires to the sample have very low contact resistance.

Five pairs of NbTi (d = 0.004") wires were also used for electrical connection of the thermometers T_H , T_C , T_L , T_R , and T_S to the conductance bridges.

b)Thermal connection:

The sample was thermally connected to the dilution refrigerator by a pure annealed polycrystalline wire of silver. For better

thermal conduction, the ends of this Ag wire were spotwelded to the sample and to the mixing chamber of the refrigerator.

A separate thermal line (silver wire) was employed for connecting the thermometer T_S , in the magnetic field to the reference thermometer which was sitting out of the magnetic field.

c) Mechanical Connections:

As was mentioned above, the mechanical stability of the sample inside the magnet was very important, and several techniques were employed to reduce these vibrations. The sample was thermally and mechanically connected to the refrigerator by two heavy pieces of copper which were connected together as shown in Fig (2.5). For better thermal conductivity, all the contact surfaces on the sample and on the copper pieces were gold plated. To produce enough pressure on the contact surface between the two copper pieces, and between the sample and the copper piece to which it was attached, brass screws were used to connect them together. In contacts with poor pressure (e.g. clamp contacts to the thermometers), the contact surfaces were wetted with Apiezon N-grease. On contacts with good pressure, the use of Apiezon N-grease was avoided.

1085; 208*2*5

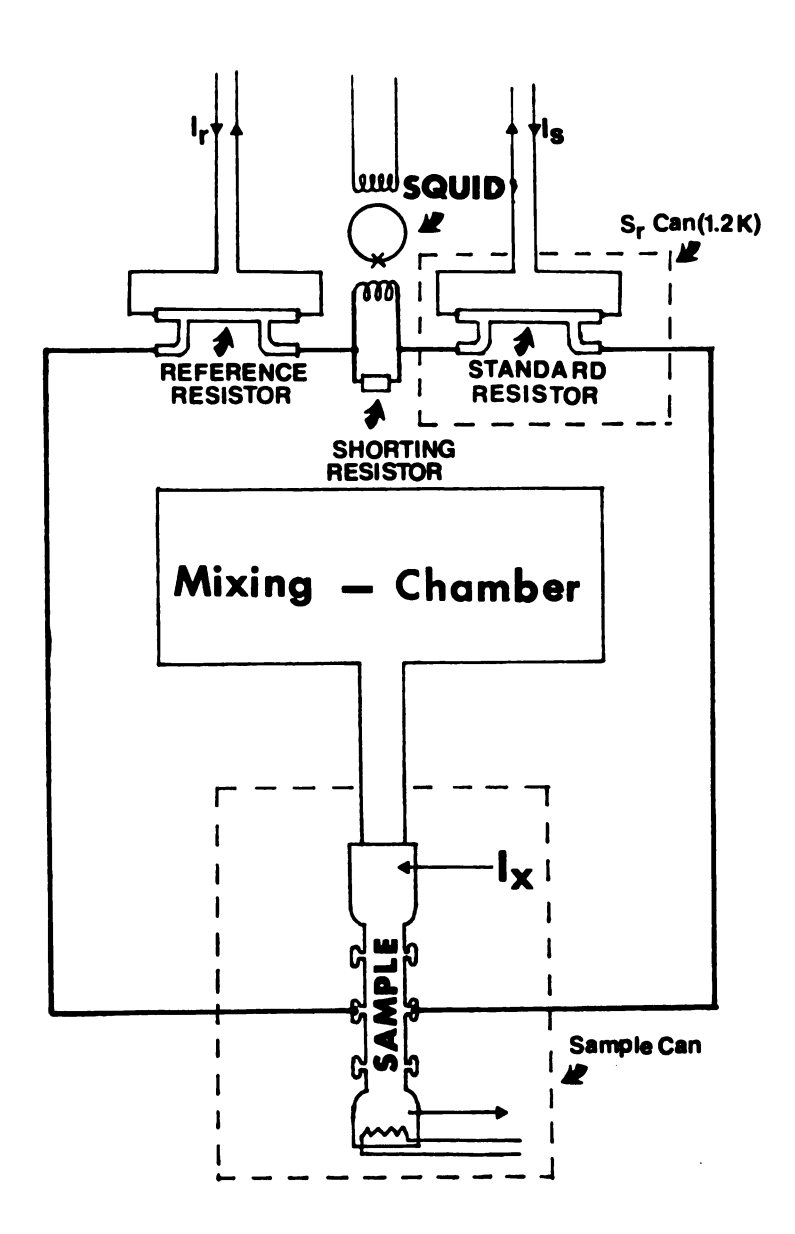


Figure (2.7)Schematic diagram of the electrica; circuit containing the Al sample for Nernst Ettingshausen and Hall coefficient measurements.

(2.7.5)Electrical Contacts to the Sample:

An important sources of noise in the SQUID loop Figure (2.7) is Johnson noise. Johnson noise is proportional to \sqrt{R} , where R is the total resistance in the SQUID loop. Since the leads in the SQUID loop are all superconducting, and the sample resistance is small, the contact resistances can make a substantial contribution to R. Consequently it was important to keep the contact resistances between the leads and the sample, and between the leads and the reference resistor as low as possible.

Different techniques for connecting the superconducting leads to the sample such as: spotwelding, soldering Indium, and plating were studied, and the resulting contact resistances were measured at Helium temperature. The plating technique provided the solution to our problem. Different kinds of solders were also used, and the contact resistances as a function of magnetic field at Helium temperature were measured. The results of these investigations are as follows.

a)Spotwelding:

After the sample was annealed and glued to the substrate, the leads were spotwelded to the sample. The spotwelding machine was an Ewald instruments model P10-10S2. Tungsten electrodes were used. The best voltage for welding the NbTi (0.004") superconducting wires

with copper clading onto the 2 mil thick Aluminum sample was found to be between 310 to 320 Volts. Because only one side of the sample was available to us (the other side was glued down to the vespel substrate), two ways for welding were tried. It was found experimentally that each technique had some advantages over the other. In both welding techniques, the two electrodes were brought down to the sample from one side. In technique (A), where both electrodes were sitting on top of the wire, the copper clading on the superconducting wire was melted first, and welded to the sample to give very good mechanical contact. On the other hand, in technique (B), where one of the electrodes was sitting on the wire while the other was sitting on the sample, only the Aluminum was melted (melting point for Al is 933K and for copper is 1356K). In technique B, the electrical resistances of the contacts were measured to be less than the electrical resistances of the contacts made by technique A. A combination of both technique (A) and (B) on several points on the sample gave the best combination of good mechanical and electrical contacts. Using this technique we made some contacts with contact resistances as low as a few un at 4.2K.

b)Soldering Indium:

Using Indalloy solder (Ref. 52) (solder #6 and flux #3), we were able to solder the NbTi leads to the sample with contact resistances as low as $1\mu\Omega$. The problem with this technique was that the flux #3 was so corrosive that the whole process of soldering had to be finished in a few seconds and then the flux had to be cleaned

immediately. Otherwise it would dissolve the sample limbs after a short time. Consequently, if the soldering of all six contacts to the sample was not completed in the first attempt, then there was no chance for a second try, and the whole process had to be repeated from the beginning on a new annealed sample.

c)Plating:

The technique of plating the sample limbs for better electrical and thermal contacts to the sample was developed by R. M. Mueller et al (Ref. 53). In this technique the sample limbs were first plated with Zinc, then Copper, and finally with Gold, as described below. Similar plating was done on the two ends of the sample, where good electrical and thermal contacts were needed. Before plating, the sample surfaces were covered with a plastic coating where the plating was not required). After plating the sample limbs, the sample was annealed and then gently mounted on its substrate. Finally using Woods metal (50% Bi, 12.5% Cd, 25% Pb, 12.5% Sn), the leads were soldered to the sample limbs. In this technique the contact resistances between the superconducting leads and the sample was measured to be less than $0.5\mu\Omega$.

The following minor changes from the technique developed by R. M. Mueller et al (Ref. 53) were made for plating Zinc and Copper onto the sample. These changes gave better experimental results.

Before electroplating the aluminum sample limbs, first the surfaces where plating was not required were covered with a plastic spray paint. Then the sample was thoroughly rinsed in distilled water and the following steps were done one after the other. Between each of these steps the Aluminum was again rinsed with water.

- 1) The sample limbs were washed with Acetone, then with Ethyl Alcohol a few times, and then the sample was dipped in water.
- 2) The sample was washed in alkaline cleaner at 75° C for 60 seconds. (Alkaline cleaner was made by mixing 11 grams of Na₃PO₄ 12H₂O and 11 grams of Na₂CO₃ and add in water to give 500 mL).
- 3) Then the sample was placed in an HNO_3 acid bath for 15 seconds. (The acid was made from 250 mL of concentrated Nitric acid in equal volume of water).
- For Zinc plating, the sample was placed in Zincate solution for 60 seconds at room temperature. (The Zincate solution was made by solving 262 grams of NaOH, 5 grams of C₄H₄KNaO₆·4H₂O, 50 grams of ZnO and .5 grams of Fecl₃·6H₂O in water and water was added to give 500 mL).

Then the sample was alternatively placed in the ${\rm HNO}_3$ acid bath for 30 seconds and the Zincate solution for 60 seconds, until the

Aluminum was slightly but uniformly etched. The zinc plating of Aluminum was the most difficult part of this technique. A slight impurity in the solutions or dirt on the Aluminum surface made the Zinc plating non-uniform. The electrocopper plating of the sample was next. The solution for copper plating was made by adding 20.6 grams of copper cyanide, 25.4 grams of sodium cyanide, 15 grams of sodium carbonate and 30 grams of C₄H₄KNaO₆·4H₂O to enough water to give 2000 mL. A piece of clean copper plate was shaped in form of a cylinder for the anode, and the sample was connected to the cathode and hung in the center of the cylinder. A current of 50mA/cm² for the first two minutes and 24mA/cm² for the next four minutes was required for copper plating at room temperature.

For Gold plating, exactly the same technique as (Ref. 53) was used.

For the plating technique, the sample preparation steps did not have the same order as the other two techniques. In this technique the sample was first cut, then plated, and finally annealed.

Since handling of a very thin annealed sample like Aluminium is very difficult, the first thing we did after annealing the sample was to glue it down to a substrate. The substrate was Vespel 1mm thick, 1cm wide and 3cm long. Vespel has a very poor thermal conductivity so that even with the very thin samples we used, the amount of heat going through the substrate is only a few percent of the total heat going through the Aluminium sample. As mentioned,

the potential leads are Nb-Ti which were twisted together so that the effective cross section of the loop developed by the leads is very small. Then the twisted wires were wetted with Apiezion N-Grease and pushed through a Pb tube. This tube was glued and anchored thermally to the mixing chamber (cold post).

(2.7.6)Magnetic Field and Current Density Dependance of Different Solders:

The magnetic field and electrical current density dependance of the electrical resistivities of several different solders were studied: Woods metal (Pb 25%, Sn 12.5%, Bi 50%, Cd 12.5%); Roses Alloy (Pb 25%, Sn 25%, Bi 50%); Tin (Sn); Indalloy (In); and Lead (Pb) were measured at 4.2K.

The arrangement for these studies is shown in Figure (2.8). The magnetic field as a function of distance from the center of the magnet is drawn on the side. The magnetic field at point (A) was always below the critical value for the solder used at this point. Therefore the contacts at point (A) were superconducting at all times while the blob of solder at point (B) at the center of the magnet was under test. Between points (A) and (B), NbTi superconducting wires were shielded in superconducting Pb ($T_c \sim 7$ K) tubing.

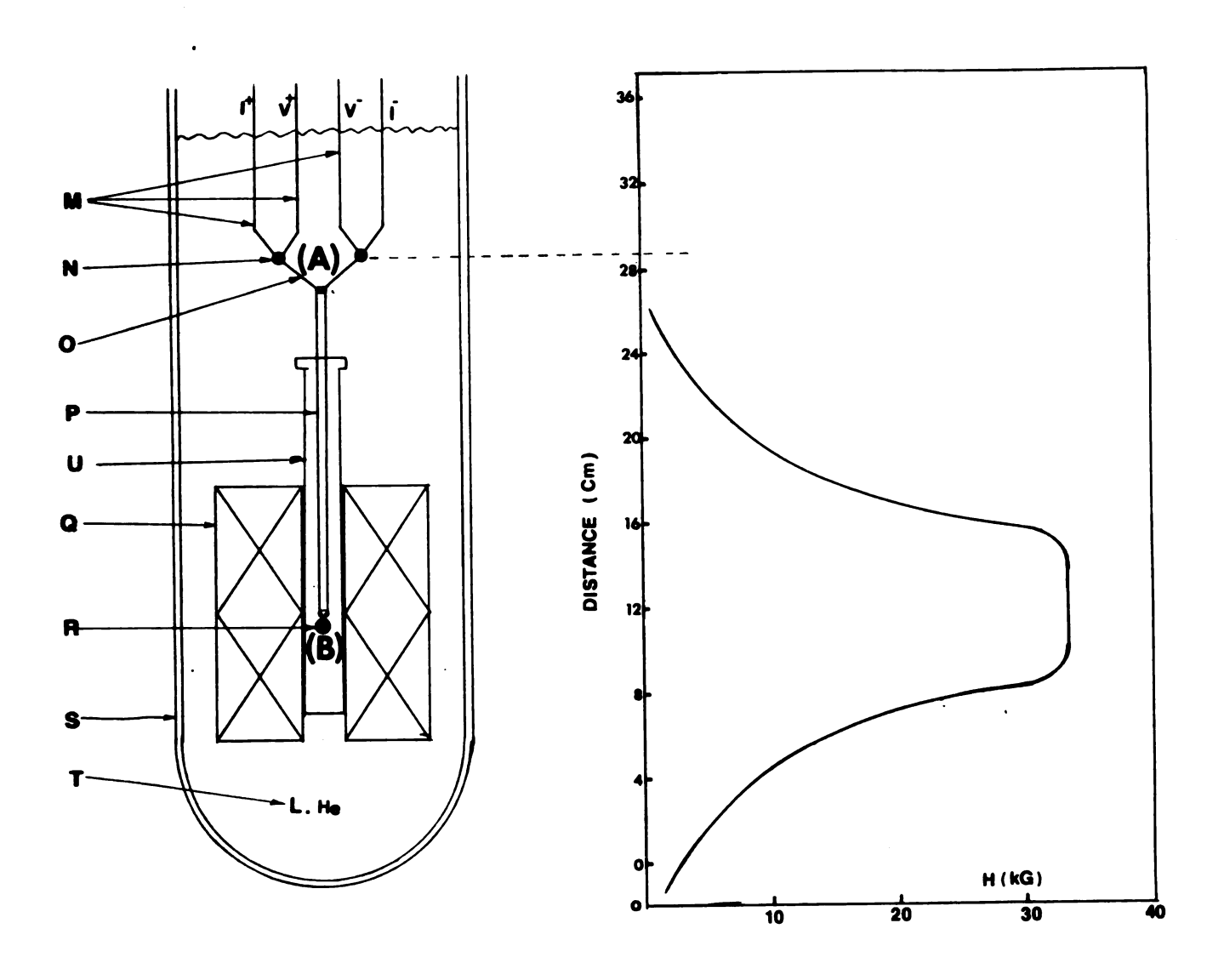


Figure (2.8a)Schematic diagram of the set up for magnetic field and current density dependance studies of different solders. (A)-Electrical connections out of the magnetic field. (B)-Solder under test inside the magnetic field. M-Voltage and current leads. N-Electrical contacts. O-Superconducting leads. P-Pb tube. U-Sample can. Q-Superconducting magnet. R-Solder under test. S-Helium dewar. T-Liquid Helium.

Figure (2.8b) Magnetic Field Distribution.

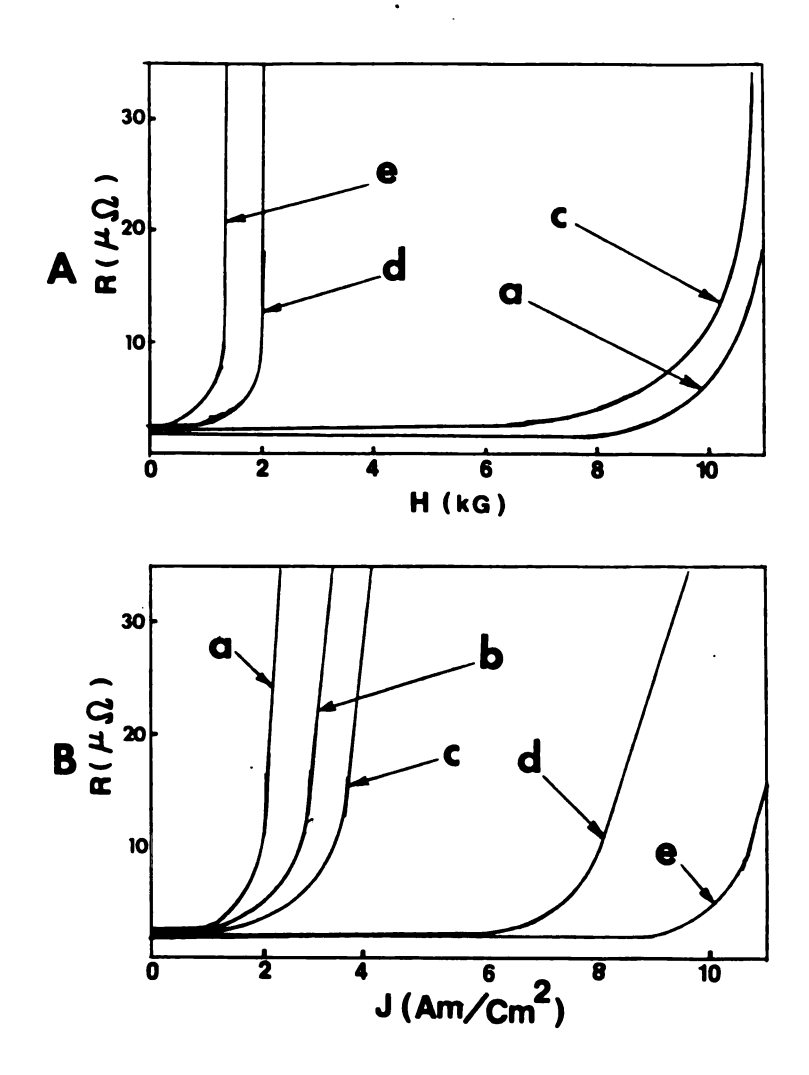


Figure (2.9)A-The magnetic field dependence of the contact resistance. B-The current density dependence of the contact resistance a) Woods metal, b) Sn, c) Roses Alloy, d) In, e) Pb.

A plot of the data is shown in Figure (2.9).

From these measurements we conclude that Rose's Alloy and Woods metal were good solders for high magnetic field and low electrical current densities, while Pb and Sn were good for low magnetic field and higher electrical current densities.

(2.7.7)Sample Can:

The sample was shielded by the sample can from the Stefan-Boltzmann thermal radiation (σT^*) of the vacuum can which was sitting in the Helium bath. The sample can and, in general, all the material used inside the magnet should be non-magnetic. Also, eddy currents due to changes in magnetic field will produce heat (Joule heating) in good electrical conductors. Therefore the sample can shouldn't be made of a good electrical conductor. On the other hand, since it is a thermal radiation shield, it should have good thermal conduction so it stays at a uniform temperature. Considering the Wiedemann-Franz law ($\frac{K}{\sigma T} = L_o$), there is a conflict between the above conditions.

To satisfy all the above conditions, the sample can was made in two different layers which were thermally anchored together. The first layer was made of stainless steel tubing with a brass top. The second layer was made of copper wires for good thermal conduction. To minimize Eddy currents, the copper wires were all

parallel to the magnetic field. The sample can is shown in Figure (2.1) and (2.8).

Because the sample can at temperature of 100 mK was closely fitted inside the vacuum can at temperature of 4.2K, it was possible that they might touch each other. To check for contact, a small copper cup, which was fitted on the end of the sample can, but electrically isolated from it, was used. After closing the vacuum can, the contact between the sample can and the vacuum can was checked through a thin wire soldered to the copper cup. By pushing the vacuum can in different directions very gently, and monitoring the electrical contact between the copper cup and the vacuum can, contact between the two cans could be detected. By adjusting the appropriate screws on the centering device, the sample can was centered inside the vacuum can.

(2.8) SUPERCONDUCTING MAGNET

(2.8.1)Introduction:

The magnetic field was produced by a 50kG superconducting magnet, purchased from Oxford Instruments Company (Model K1034) The magnet had inner and outer winding radii of 2.98 cm and 4.71 cm, respectively, with a winding length of 6.20 cm. The homogeneity of the magnetic field in the z-direction over the center 1" was 0.1%. The power supply for the magnet was Hewlett Packard, (model # Harrison 6260A), which was controlled by a ramp current controller made by Eastern Scientific. At the geometric center of the magnet

the magnetic field changed linearly with the current at a rate of 848.9 Gauss per Ampere. A superconducting switch in parallel with the superconducting magnet, allowed us to operate the magnet in a persistent mode with the power supply disconnected. This switch was operated by a heater with an internal impedance of 110 Ohms. To turn off the superconducting switch, 40mA was applied to its heater. X and y trim coils on the magnet provided fine adjustment of the direction of the magnetic field.

The superconducting wires were Niomax A61/40 (niobium titanium), and the maximum energizing rate of the magnet was 30 Amps/minute. The maximum applied voltage was 4 Volts and the maximum safe operating current was 58.9 Amps. which produced 50 kG. The magnet quenched for currents over 65 Amps.

(2.8.2) Electrical Connections to the Superconducting Magnet:

For carrying a current of ~50 A into the Helium bath to supply the magnet, insulated Cu wires of about 0.5 cm² cross section were used in the region outside the cryostat. We did not want, however, bring such thick wires all the way down into the liquid helium, since they would conduct too much heat into the liquid. To minimize the heat conduction into the liquid, we want the wires to be as thin as possible. However, for a given current, thinner wires produce greater Joule heating, which boils off more liquid helium. If we required the thin wires to go from room temperature to 4.2K, we found that if the wire thickness was large enough to carry 50A, then the heat conducted down the wire was significantly larger than the

Joule heat produced in the wire. After bringing the thick Cu wires into the cryostat through sealed connectors, we therefore wrapped them around a cylindrical copper heat sink in the helium gas at the top of the cryostat, and cut the wires off about 5 cm beyond the end of the heat sink. This brought the cut ends to well below room temperature, and allowed us to keep the leads that went into the liquid relatively thick, thereby minimizing Joule heating. We found that a set of Cu wires with total diameter of 2.5 mm going into the liquid still gave an acceptably low extra He boiloff rate (about liters/hour), yet was thick enough to ensure that the wires would not burn through during the measurements. Superconducting leads were soldered in parallel to the thin Cu wires over a substantial portion of their mutual lengths, so that both Cu and superconducting wires would be carrying both current and heat for a wide range of liquid helium depths. The Cu leads ended just above the top of the superconducting magnet.

(2.8.3)Pressure Relief Valves:

The superconducting magnet is in the Liquid Helium bath, and usually operates in a closed superconducting loop through a superconducting switch. If during operation, the level of the Liquid Helium falls so low that a portion of the superconducting magnet turns normal, or, if the magnetic field is swept too rapidly, then the magnet quenches. As the result of this quenching many liters of liquid Helium evaporate at once. In order to save the Helium glass dewar from excessive over-pressure during a quench

accident, two pressure relief valves Figure (2.10) were designed and mounted on top of the cryostat. As is shown in Figure (2.10): i)—these valves have a large opening (~1" in diameter); ii)—the minimum relieve pressure is adjustable by changing the weights on top of the valve; and iii)—The o-ring produces a high-vac seal pressures below 1 Atmosphere. These valves were capable of releasing many liters of Helium in a few seconds.

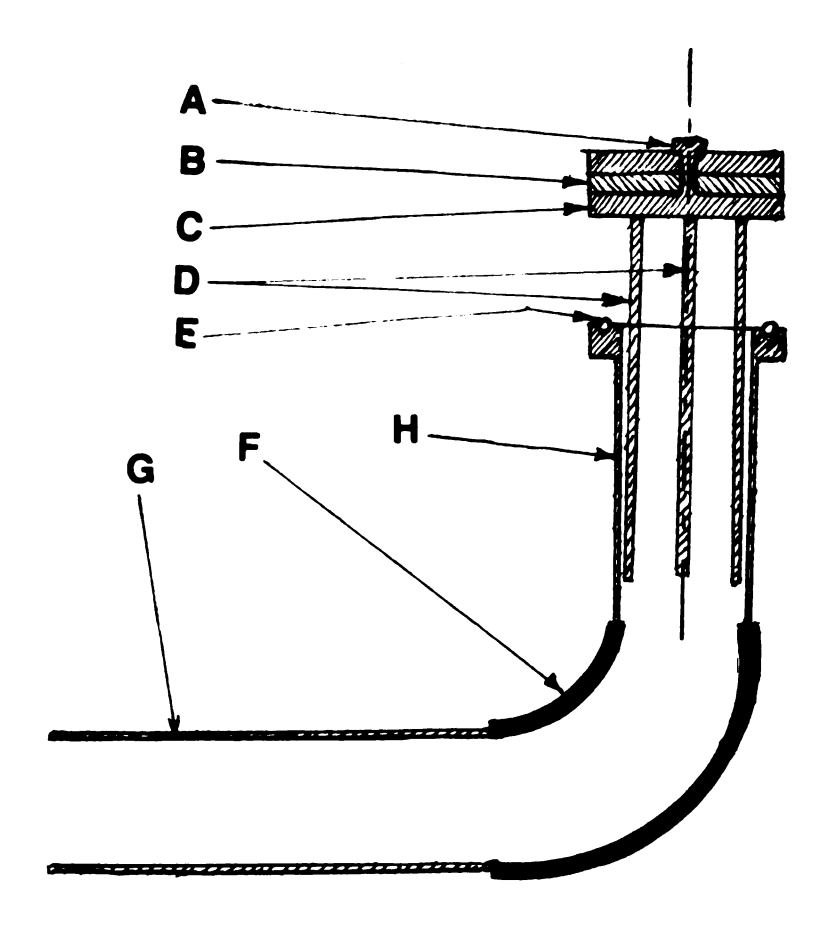


Figure (2.10)Helium pressure relief valve: A-Weight holder screw. B-Extra weights. C-Top flange. D-Top valve holder. E-O-ring seal. F-Elbow. G-Brass pipe. H-Copper pipe casing.

(2.9) Reference Resistor:

In order to get optimal precision in the SQUID circuit, the noise of the reference resistor must not be larger than that of the sample. Different factors such as Johnson noise, magnetic field dependence (magneto resistance), temperature dependence, current dependence, and thermoelectric voltage noise due to temperature fluctuations, affect the accuracy and the precision of a measurement. In order to keep the SQUID in a stable state and make full use of the precision of the current comparator, the resistance of the reference resistor should be close to the resistance of the sample.

A good reference resistor with low magnetoresistance, low temperature dependence, low current dependence, low thermopower, stable resistance upon thermal cycling and especially low noise (noise due to the vibration of its leads in the magnetic field) is difficult to make. The reference resistor was made from silver wire with 0.4% Platinum impurity as shown in Figure (2.7). At Helium temperature the resistance of the reference resistor was 8.78×10^{-6} Ω and its Johnson noise with the assumption of $\Delta f = 1$ Hz, was about 4×10^{-14} Volts. Since this Johnson noise was much smaller than the voltage sensitivity required for NE measurements, there was no need to lower the temperature of the reference resistor in order to lower its Johnson noise. Consequently the reference resistor was mounted inside the Helium bath at 4.2K, which had the great advantage of allowing it to be far away from the superconducting magnet.

The reference resistor was mounted inside a superconducting switching box which allowed it to be switched in or out of the SQUID circuit. This switching box provided us with several alternative superconducting connections to the SQUID circuit for different experiments, Figure (2.11). The superconducting connections, the reference resistor, and the shorting resistor for the SQUID, were all shielded from the magnetic field inside the superconducting box. Since the reference resistor was out of the magnetic field, and at Helium temperature, the effects of magneto-resistance, temperature dependence, thermopower, and especially the noise due to the vibration of the leads in the magnetic field, were minimized.

(2.10)SQUID's in a Feedback Loop:

As described earlier in this chapter, a SQUID was used as the null detector for very small voltage measurements. During the experiment, in order to keep the SQUID locked, we ramped up two currents simultaneously, one through the sample (called the master current) and the other through the reference resistor (called the slave current). This procedure ensured that the voltage produced in the sample by the master current stayed closely equal to the voltage roduced in the reference resistor by the slave-current, so that the SQUID remained balanced near zero voltage. For details see the circuit diagram in Figure (2.7).

For Hall coefficient measurements, where the sample voltage is linearly dependent on the master current, the current comparator can ramp up the two currents (master and slave) together, and the SQUID

remains locked. From measurement of the ratio of slave to master currents, and from the known value of reference resistor, the sample voltage can be evaluated.

For thermoelectric measurements, in contrast, the voltage of interest is not linearly dependent on the input current (e.g. the NE coefficient is proportional to U_{X} , the thermal current density, and U_{X} in turn is proportional to I^2 , the square of the current), and this procedure doesn't work if the voltage is too large. . In this case, we used the SQUID in a feedback loop as shown in Figure (2.11). Here, one current (usually the master current) was ramped up from zero to its maximum value, while the other (slave) current was controlled by electronic feedback to keep the SQUID locked (i.e the voltage on the SQUID remains zero) during the ramping process. Above 1K, this procedure was necessary for NE measurements. However, at .147K, the transverse voltage was so small that the current comparator technique could be used to measure the NE coefficient.

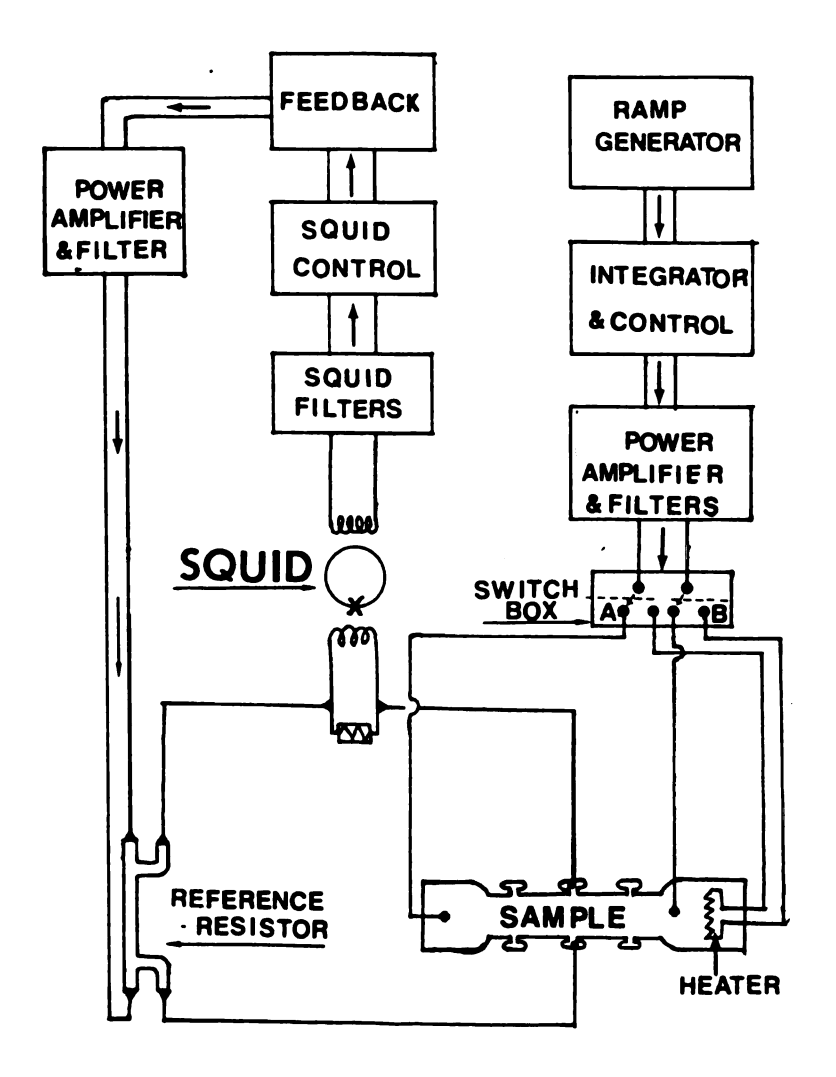


Figure (2.11)Simplified block diagram of the SQUID circuit in a feedback loop, for measuring i-switch position (A), Hall coefficient ii-switch position (B), Nernst Ettingshausen coefficient.

CHAPTER 3

THEORY

In this chapter the theory of electronic transport is reviewed; especially the off-diagonal element of the transport tensor which is expected to be subject to many body renormalization involving the electron-phonon mass enhancement. First, the basic idea of electron-phonon mass enhancement is described. Second, the fundamental transport equations and their tensor coefficients are written out, and the relations between the tensor coefficients are described. Third, transport in high magnetic field is discussed, and the magnetic field dependences of the transport tensor coefficients are derived. Finally the high magnetic field Nernst-Ettingshausen coefficient is derived for compensated and uncompensated metals.

(3.1)Electron-Phonon Mass Enhancement::

Crudely speaking, as an electron moves through the lattice, it attracts nearby positive ions by Coulomb attraction and tries to drag these positive ions along with it. This is equivalent to an increase in the electron's effective mass. By dragging the ions along, the electron distorts the lattice in its close neighborhood. This distortion is felt by other electrons because of the long range Coulomb interaction. Therefore the electrons are coupled together

by this lattice distortion, which can be viewed as an electron-phonon interaction. For electrons which are weakly coupled together, we get a system of non-interacting quasi-particles with the same wave vectors, \vec{k} , as the original electrons, but with a perturbed energy $\vec{E}(\vec{k})$, given by the Brillouin-Wigner (Ref.55) perturbation equation (note that $\vec{\epsilon}$ is the thermoelectric tensor, \vec{E} is the electric field, and finally \vec{E} is the energy of the electron.)

$$E(\vec{k}) = E_{O}(\vec{k}) + \Sigma(E(\vec{k}), \vec{k})$$
 (3.1)

where $E_0(k)$ is the unperturbed band energy of the electron and $\Sigma(E(k),k)$ is the electron self energy due to electron-phonon interactions.

We now consider the transport properties of these quasi-particles. The transport properties of quasi-particles which at low temperature are elastically scattered by a random distribution of impurities may be described in terms of a mean free path $\vec{l}(\vec{k})$. This mean free path is related to the renormalized relaxation time $\tau(\vec{k})$, by

$$\vec{1}(\vec{k}) = \vec{V}(\vec{k}) \cdot \tau(\vec{k})$$
 (3.2)

where $\vec{V}(\vec{k})$ is the velocity of a quasi-particle in state \vec{k} , and is defined as:

$$\vec{V}(\vec{k}) = \frac{1}{\hbar} \vec{\nabla}_{\vec{k}} E(\vec{k})$$
 (3.3)

For non-interacting electrons we have

$$\vec{V}_{O}(\vec{k}) = \frac{1}{\hbar} \vec{\nabla}_{\vec{k}} E_{O}(\vec{k})$$
 (3.4)

From equation (3.1) we see that,

$$\vec{\nabla}_{\mathbf{k}} E(\vec{k}) = \vec{\nabla}_{\mathbf{k}} E_{0}(\vec{k}) + \frac{\partial \Sigma}{\partial E(\vec{k})} \vec{\nabla}_{\mathbf{k}} E(\vec{k}) + \frac{\partial \Sigma}{\partial k}$$
(3.5)

or by rearrangement of terms and multiplying by $\frac{1}{h}$:

$$\frac{1}{\hbar} \vec{\nabla}_{k} E(\vec{k}) = \frac{\frac{1}{\hbar} \vec{\nabla}_{k} E_{O}(\vec{k})}{(1 - \frac{\partial \Sigma}{\partial E(\vec{k})})} + \frac{\frac{1}{\hbar} \frac{\partial \Sigma}{\partial k}}{(1 - \frac{\partial \Sigma}{\partial E(\vec{k})})}$$
(3.6)

Substituting equations (3.3) and (3.4)into eg (3.6) and defining the mass enhancement parameter λ as

$$\lambda(\vec{k}) = -\frac{\partial \Sigma(E(\vec{k}), \vec{k})}{\partial E(\vec{k})}$$
(3.7)

We get

$$\vec{V}(\vec{k}) = \frac{\vec{V}_0(\vec{k})}{1 + \lambda(\vec{k})} + \frac{\frac{1}{\hbar} \frac{\partial \Sigma}{\partial k}}{1 + \lambda(\vec{k})}$$
(3.8)

The term $\frac{1}{h} \frac{\partial \Sigma(E(k),k)}{\partial k}$ is defined as

$$\frac{1}{h} (\vec{k}) = \frac{1}{h} \frac{\partial \Sigma(E(k), k)}{\partial k}$$
(3.9)

The quantity $\Sigma(E(\vec{k}), \vec{k})$ varies very slowly with respect to \vec{k} , and $\vec{\eta}(\vec{k})$ is much smaller than $\vec{V}_{0}(\vec{k})$ (Ref. 55), and in most cases can be neglected. However, $\vec{\eta}(\vec{k})$ varies much more rapidly with energy near the Fermi energy than does $\vec{V}_{0}(\vec{k})$ (ref. 55). Since, the diffusion thermopower depends upon energy derivatives (see the Mott Rule later in this chapter), $\vec{\eta}(\vec{k})$ can make a significant contribution to the thermopower as first pointed out by Lyo (Ref. 55).

Since for a metal $\lambda(\vec{k})$ is positive at the Fermi energy E_F (Ref. 56), the quasi-particles, as we expected from the elementary picture of the electron-phonon interaction, have lower velocities than non-interacting electrons.

The density of states in the band is given by the general form of,

$$N(E) = \int_{S(E)} \frac{dS}{4\pi^3} \frac{1}{\left| \vec{\nabla} E(\vec{k}) \right|}$$
 (3.10)

Where the integral is over the constant energy surface S(E).

 $\vec{\nabla}_{\vec{k}} E(\vec{k})$ is proportional to $\vec{V}(\vec{k})$ (eq. 3.3), and the Fermi Surface is not affected by mass enhancement (Ref. 56). Thus, if $\lambda(\vec{k})$ is independent of \vec{k} , then the electronic density of states at E_f is

$$N_C(E_F) = (1 + \lambda) N_C^O(E_F)$$
 (3.11)

where $N_c(E)$ and $N_c^0(E)$ are the enhanced and unenhanced electronic density of states. The electronic density of states as a function of energy is shown in Figure (3.1).

In terms of the dispersion relation, this enhancement has the effect of producing a different slope in the vicinity of E_F as shown in Figure (3.2). This slope is equal to $\frac{\partial E}{\partial k}$, and if we define m*, from equation (3.3) as (57)

$$\frac{1}{\hbar} \overrightarrow{\nabla}_{k} E \Big|_{E_{F}} = \overrightarrow{V}(\overrightarrow{k}) \Big|_{E_{F}} = \frac{\hbar \overrightarrow{k}}{m^{*}}$$
 (3.12)

then the slope at E_f is

$$\frac{\partial E}{\partial k}\Big|_{E_{F}} - \frac{1}{m^{*}} - \sqrt[3]{(k_{F})} = \sqrt[3]{(k_{F})/(1+\lambda)}$$
(3.13)

which is $(1 + \lambda)$ times smaller than the slope for the non-interacting electron model. Using the same definition as above for the non-interacting electron model

$$\frac{\partial E_{O}}{\partial k} \left| E_{F} - \frac{1}{m} - V_{O}(k_{F}) \right| \tag{3.14}$$

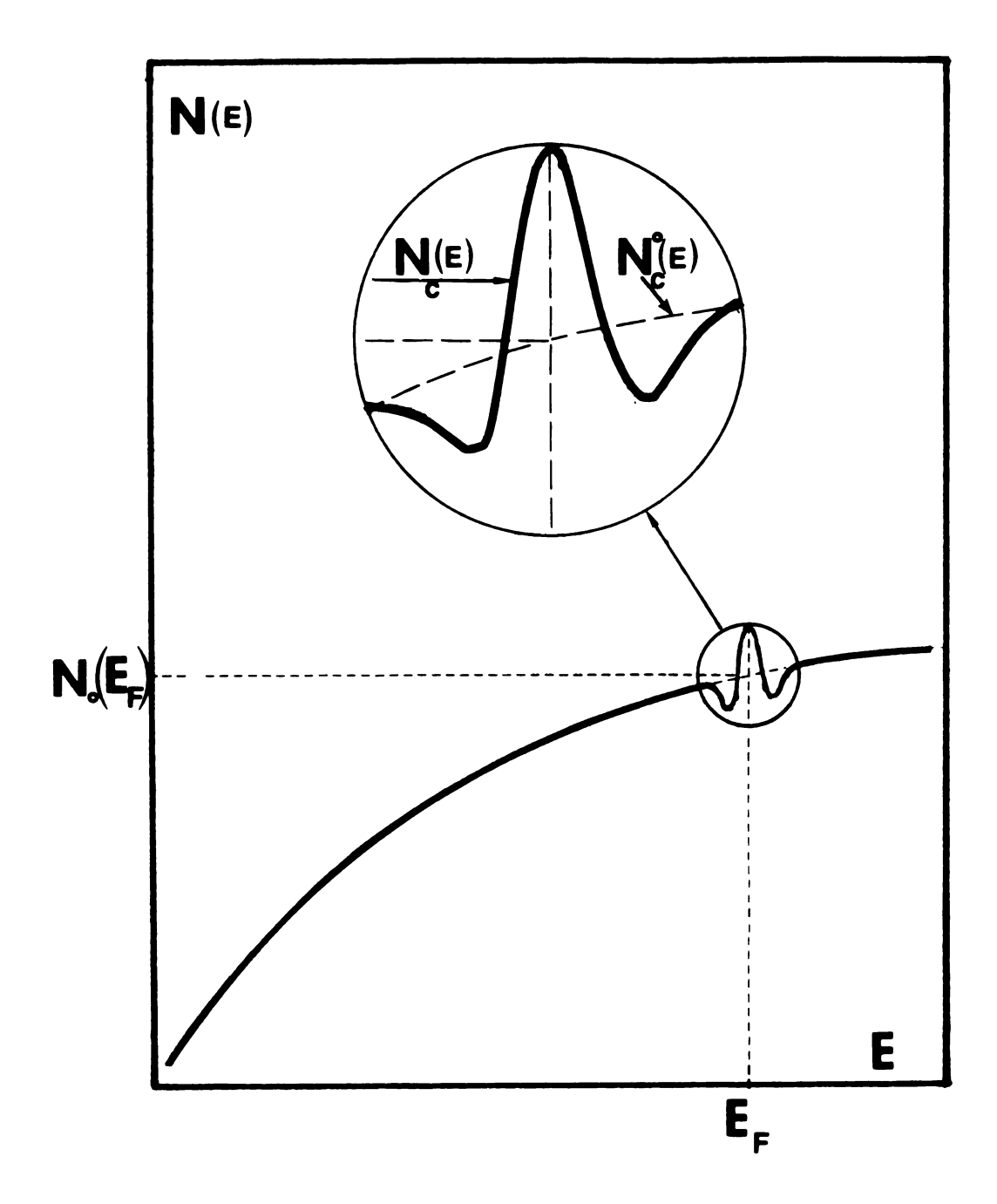


Figure (3.1)Electronic density of states as a function of energy, where N $_{\rm C}$ (E) and N $_{\rm C}^{\rm O}$ (E) are the enhanced and unenhanced electronic density of states.

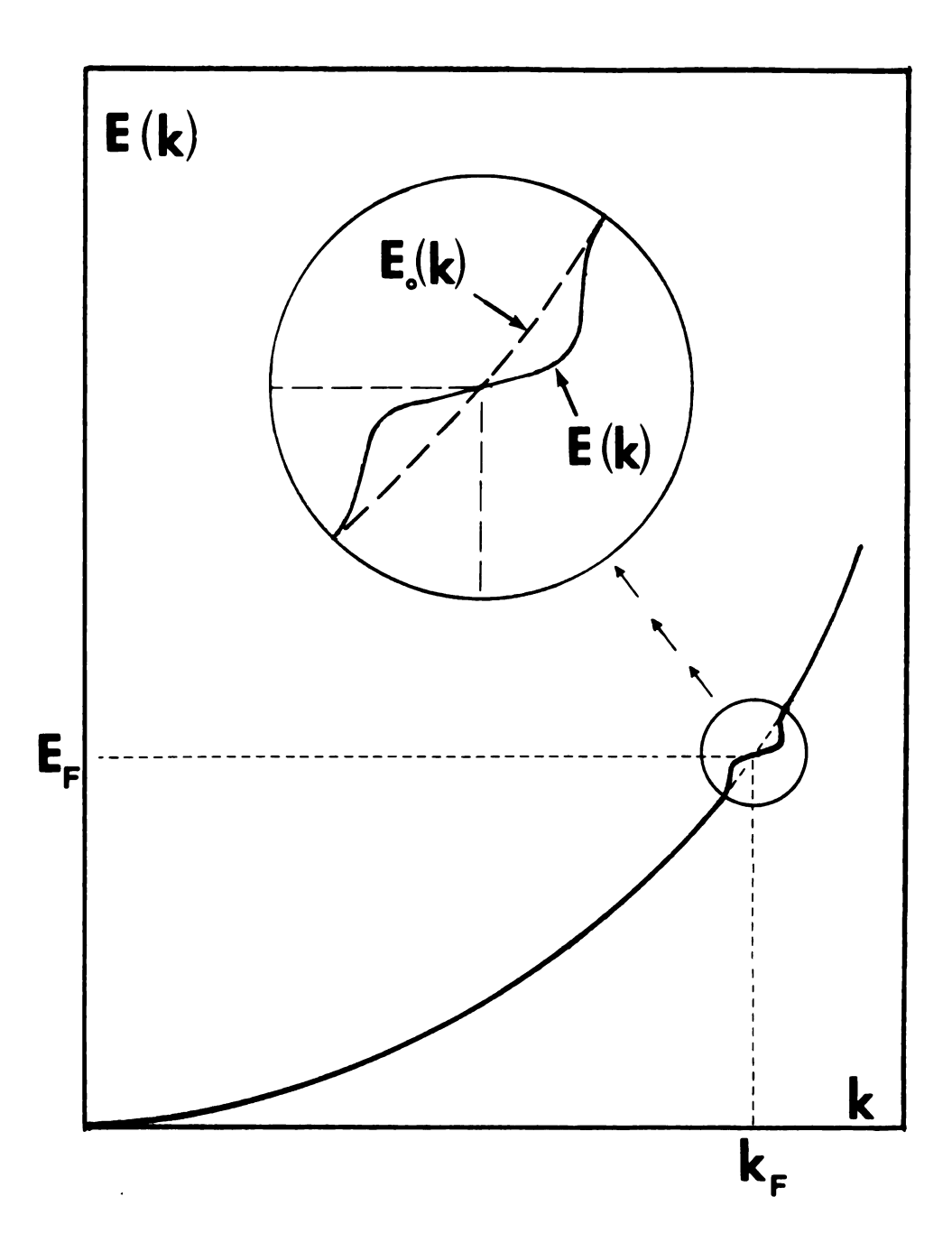


Figure (3.2)The dispersion relation, E(k) for enhanced and $E_0(k)$ for unenhanced electrons. The enhancement has the effect of producing a different slope in the vicinity of E_f .

We conclude that

$$m^* = m(1+\lambda) \tag{3.15}$$

Qualitatively, as noted above, one can think of the electron having to drag along a phonon cloud, which thereby slows its motion down and increases its mass.

If, in addition, we think of the mean free path for scattering by impurities as 'roughly' the distance between impurities, then the mean free path will be uneffected by the fact that the electron is slowed down; i.e.

$$\vec{1}(\vec{k}) - \vec{1}_{0}(\vec{k})$$
 (3.16)

Then since $l = V\tau$, we must have

$$\tau(\vec{k}) = \tau_0(\vec{k}) (1 + \lambda) \tag{3.17}$$

Here, $\tau(\vec{k})$ and $\vec{l}(\vec{k})$ are the perturbed (renormalized) and $\tau_0(\vec{k})$ and $\vec{l}_0(\vec{k})$ are the unperturbed relaxation time and the mean free path between the scatterings, respectively.

Finally, as mentioned in the introduction the electronic specific heat is linearly proportional to the electronic density of states [eq 1.8)], and the specific heat has been shown (Ref. 6) to be enhanced by the same factor as the density of states.

With this background, we now turn to the fundamental transport equations and define the proper coefficients for compensated and

umcompensated metals in order to look for the electron-phonon mass enhancement.

(3.2) Fundamental Transport Theory:

The electrical current density and the heat current density are defined as

$$\begin{cases}
\vec{J} = \int e \vec{V} \cdot f(\vec{k}) \cdot d\vec{k} & (3.18) \\
\vec{U} = \int (E - \mu) \cdot \vec{V} \cdot f(\vec{k}) \cdot d\vec{k} & (3.19)
\end{cases}$$

where $f(\vec{k})$ is the electron distribution function and μ is the chemical potential. The electron distribution function $f = f(\vec{k})$ can be evaluated by solving the Boltzmann Transport Equation (BTE), which in metals can be written as (Ref. 56)

$$-\vec{k} \cdot \vec{\nabla}_{k} f - \vec{V} \cdot \vec{\nabla}_{r} f = -(\frac{\partial f}{\partial t})_{\text{scatt}}$$
 (3.20)

Here $\frac{\partial f}{\partial t}$)_{scatt}, is the rate of change of the distribution function due to scattering, and k is the partial derivative of k with respect to time.

If we take the solution f(k) of Eqn. (3.20) which is linear in E and ∇T , then by substituting this solution into equations (3.18) and (3.19) we obtain the macroscopic transport equations. These

equations are written in two different forms with different tensor coefficients. Since in this study we are dealing with tensor coefficients from both forms of the transport equation, we explain each briefly.

The first form of the transport equations were given in the introduction:

$$\begin{cases}
\vec{J} = \vec{\sigma} \cdot \vec{E} + \vec{\epsilon}'' \cdot (-\vec{\nabla}T) \\
\vec{U} = \vec{\epsilon} \cdot \vec{E} + \vec{\lambda} \cdot (-\vec{\nabla}T)
\end{cases} (3.21)$$

where from the Onsager relations (Ref. 2)

$$\stackrel{\leftarrow}{\epsilon} = T \cdot \stackrel{\leftarrow}{\epsilon}".$$
 (3.23)

The second form of transport equations are

$$\begin{cases}
\vec{E} = \overrightarrow{\rho} \cdot \vec{J} + \overrightarrow{S} \cdot \vec{\nabla}T \\
\vec{U} = \overrightarrow{\pi} \cdot \vec{J} - \overrightarrow{\lambda}^{\dagger} \cdot \vec{\nabla}T
\end{cases} (3.24)$$

 ρ = The electrical resistivity tensor

 \dot{S} = The thermopower tensor

 π = The Peltier tensor

 λ^{+} = The thermal conductivity tensor

Where from the Onsager relations π = T S, and

$$\lambda = \lambda'' + T \frac{\dot{\epsilon}''}{\dot{\epsilon}}$$
 (3.26)

All of the above tensor coefficients are functions of temperature and magnetic field. We note that with either form of the transport equations, four coefficients would normally be needed to relate \vec{J} and \vec{V} to \vec{E} and \vec{V} . However the Onsager relations reduce the number of independent coefficient tensors to three.

The coefficient tensors of the two forms of the transport equation are directly related together by

$$\sigma \cdot \rho = 1 = \text{Unit tensor}$$
 (3.27)

Now from the transport equation we return to the BTE for the evaluation of the tensor coefficients σ , ρ , ϵ and δ .

In a cubic metal with the magnetic field along the z-direction and also along a 3-fold symmetry direction, (Ref. 8), the tensor σ is

$$\vec{\sigma} = \begin{bmatrix}
\sigma_{xx} & \sigma_{xy} & \circ \\
-\sigma_{yx} & \sigma_{yy} & \circ \\
\circ & \circ & \sigma_{zz}
\end{bmatrix}$$
(3.29)

 $\sigma_{\mbox{ij}}$ is the ith, jth element of the conductivity tensor $\overset{\mbox{\scriptsize \sc to}}{\sigma}.$

The tensor coefficient ρ , which has a similar form as σ , can be derived in terms of σ tensor elements for a cubic metal as follows:

First write,

$$\hat{\rho} = \begin{bmatrix}
\rho_{xx} & \rho_{xy} & 0 \\
-\rho_{yx} & \rho_{yy} & 0 \\
0 & 0 & \rho_{zz}
\end{bmatrix}$$
(3.30)

Then from equation (3.20) with the boundary conditions $J_v = J_z$ = 0 and $\overrightarrow{\nabla}T$ = 0, we get

$$\begin{cases}
\vec{J}_{x} = \sigma_{xx} E_{x} + \sigma_{xy} E_{y} \\
\vec{J}_{y} = -\sigma_{xy} E_{x} + \sigma_{xx} E_{y} = 0
\end{cases} (3.31a)$$

$$\vec{J}_{x} = \sigma_{xy} E_{x} + \sigma_{xx} E_{y} = 0 \qquad (3.31b)$$

$$\vec{J}_{x} = \sigma_{xy} E_{x} + \sigma_{xx} E_{y} = 0 \qquad (3.31c)$$

$$\dot{J}_{z} = \sigma_{zz} E_{z} = 0. \tag{3.31c}$$

Combining equations (3.31a) and (3.31b), $\rho_{\mbox{\scriptsize XX}}$ and $\rho_{\mbox{\scriptsize yX}}$ can be deduced in terms of σ_{xx} and σ_{xy} as follows:

$$\rho_{xx} = \frac{E_y}{J_x} = \frac{\sigma_{xy}}{\sigma_{xx}^2 + \sigma_{xy}^2}$$
 (3.32)

$$\rho_{xy} = \frac{E_x}{J_x} = \frac{\sigma_{xx}}{\sigma_{xx}^2 + \sigma_{xy}^2}$$
 (3.33)

These two equations show that in order to determine the behaviors of ρ_{XX} and ρ_{XY} , in general we need to know the behaviors of both σ_{XY} and σ_{XX} .

The DC conductivity of a metal is simplified by Ashcroft and Mermin (Ref. 2) as follows

$$\sigma(E) = e^{2} \tau(E) \int \frac{dk}{4\pi^{3}} \frac{\partial f}{\partial E} \vec{V}(\vec{k}) \vec{V}(\vec{k})$$
 (3.34)

where the integral is over the Fermi surface in k-space.

The tensor coefficient $\stackrel{\longleftarrow}{\epsilon}$ is related to $\stackrel{\longleftarrow}{\sigma}$ by the Mott Rule (Ref. 2)

$$\dot{\varepsilon}'' = eL_OT[\frac{d\dot{\sigma}'(E)}{dE}]_{E=E_F} + \dots$$
 (3.35)

Then from equations (3.22) and (3.25) we get

$$\dot{S}^{+} = \frac{\dot{\varepsilon}^{+}}{\dot{\sigma}^{+}} = \frac{eL_{o}^{T}}{\dot{\sigma}^{+}} \left[\frac{d\sigma}{dE}\right]_{E=E_{F}}$$
(3.36)

Now that we have a general idea about the transport equations and the tensor coefficients, we focus our attention on the high magnetic field limit of such coefficients, and concentrate upon the off diagonal component of the thermoelectric tensor $\hat{\epsilon}^{\dagger}$ and, also upon the Nernst-Ettingshausen (NE), Righi-Leduc (R₁) and Hall

:2:

::

($R_{\mbox{\scriptsize H}}$) coefficients for compensated and uncompensated metals as defined in the introduction.

(3.3) Transport in High Magnetic Field:

We now show that for analysis of transport properties in magnetic field, the new variables

- E = the energy of the electron
- k_z = the component of its crystal momentum parallel to the magnetic field
- ϕ = an angular variable whose time derivative is the cyclotron frequency

are more appropriate than the variables k_x , k_y , k_z . After explaining the new variables, the Boltzmann Transport Equation is written in a new form in which $f(k_x,k_y,k_z) \rightarrow \psi(E,k_z,\phi)$. Then, in the high field limit by expanding the magnetic field dependence of ψ in a power series in $\frac{1}{H}$, (here we use the symbol H for magnetic field, so as to follow the notation in the references for the following analysis) we will find for each tensor element σ , ρ , ε , the leading (non-zero) term for a metal with a given structure: compensated or uncompensated; open or closed orbits.

The semi-classical equation of motion of a wave packet under an applied Electric and Magnetic field (Ref. 56) is

$$h \frac{d\vec{k}}{dt} = e\vec{E} + \frac{e}{c} (\vec{V} \times \vec{H})$$
(3.37)

If the electric field \vec{E} = 0, and the magnetic field is in the z-direction then,

$$\vec{H}_z \cdot (\vec{h} \frac{d\vec{k}}{dt}) = \vec{h} \frac{d}{dt} (\vec{H}_z \cdot \vec{k}) = \frac{e}{c} H_z \cdot (\vec{V} \times \vec{H}_z) = 0$$
 (3.38)

From $\frac{d}{dt}$ (\vec{H}_z • \vec{k}) = 0 we conccude that the z component of \vec{k} should be constant (\vec{k}_z = constant).

Also for the energy E we can write

$$\frac{dE}{dt} = \vec{\nabla}_{\mathbf{k}} E \cdot \frac{d\vec{k}}{dt}$$
 (3.39)

Using equation (3.37), at zero electric field, we will find that the energy is conserved (E = constant).

From E = constant and \vec{k}_z = constant we reach the conclusion that in a magnetic field only (i.e. no electric field), the electron moves in k-space along an orbit for which energy is constant at the Fermi energy, and the component of \vec{k} parallel to \vec{H} is also constant.

Of course when the electric field is not zero, the energy E and \vec{k}_z are not precisely conserved any more, but \vec{k}_z will be a function only of the electric field, and the energy will change little

compared to E_F . In this case, k_Z will still be appropriate as one of the parameters, especially in the high-field limit when the second term on the right-hand-side of equation (3.37) is much larger than the first term. In such a case, the electronic trajectory remains within a distance k_B^T from the Fermi energy and can be approximated as lying on E_F .

From equation (3.38) we also reach the conclusions that

$$\begin{cases} \frac{dk}{x} = \left(\frac{e}{hc}\right) V_y H_z \\ \frac{dk}{dt} = -\left(\frac{e}{hc}\right) V_x H_z \end{cases}$$
 (3.40)

The magnitude of $\frac{ds}{dt}$ (s is the differential path length in the k_x, k_y plane) is then given by

$$\frac{ds}{dt} = \left[\left(\frac{dkx}{dt} \right)^{2} + \left(\frac{dky}{dt} \right)^{2} \right]^{1/2} = \frac{e}{hc} H_{z} (V_{x}^{2} + V_{y}^{2})^{1/2} = \frac{e}{hc} H_{z} V$$

$$dt = \left(\frac{hc}{eH_{z}} \right) \frac{ds}{V}$$
(3.42)

In general, (t), the differential time element for motion along the trajectory is used as the third variable, and ϕ is an alternative to it in the specific case when we have a closed orbit. ϕ and t are related together by the cyclotron frequency $\omega_{_{\mbox{\scriptsize C}}}$, as

$$\frac{\mathrm{d}\phi}{\mathrm{d}t} = \frac{2\pi}{T} = \omega_{\mathrm{c}} \tag{3.43}$$

and the cyclotron frequency is related to the cyclotron mass $\mathbf{m}_{_{\mathbf{C}}}$ by

$$\omega_{c} = \frac{H}{m_{c} \cdot C} \tag{3.44}$$

We now rewrite the BTE equation in terms of new variables ϕ , E and \vec{k}_z under the conditions of applied electric field \vec{E} , magnetic field in the z-direction, and zero $\vec{\nabla}T$ for a closed orbit. Setting $\frac{\partial f}{\partial t} = \vec{\nabla}_k f = 0$ the BTE becomes,

$$\dot{\vec{k}} \cdot \vec{\nabla}_{\vec{k}}(f) = (\frac{\partial f}{\partial t})_{\text{scat}}$$
 (3.45)

In terms of the new variables, Eqn. (3.45) becomes

$$(\frac{\partial f}{\partial \phi}) \stackrel{\bullet}{\phi} + \frac{\partial f}{\partial E} \stackrel{\bullet}{E} + \frac{\partial f}{\partial k_z} \stackrel{\bullet}{k_z} = (\frac{\partial f}{\partial t})_{\text{scatt}}$$
 (3.46)

In the above equation \dot{E} and \dot{k}_z are unaffected by H $_z$ because, from equations (3.3) and (3.37)

$$\dot{\mathbf{E}} = \vec{\nabla}_{\nu}(\mathbf{E}) \cdot \dot{\mathbf{k}} = \mathbf{e} \, \vec{\mathbf{V}} \cdot \vec{\mathbf{E}} \tag{3.47a}$$

and

$$\dot{k}_z = \frac{e}{\hbar} \dot{E}_z. \tag{3.47b}$$

However,
$$\dot{\phi} = \omega_{c}$$
 is proportional to H. (3.47c)

Substitute equation (3.47a,b,c) into (3.46)

$$\omega_{c} \frac{\partial f}{\partial \phi} + e \vec{V} \cdot \vec{E} \frac{\partial f}{\partial E} + \frac{e}{\hbar} \vec{E}_{z} \frac{\partial f}{\partial k_{z}} = (\frac{\partial f}{\partial t})_{scatt}$$
 (3.48)

By change of $f \rightarrow f_{0} - \frac{\partial f_{0}}{\partial E} \psi$, we get

$$(\frac{\partial f_{o}}{\partial E}) \omega_{c} \frac{\partial \psi}{\partial \phi} + (\frac{\partial f_{o}}{\partial E}) E \vec{V} \cdot \vec{E} + (-\frac{\partial f_{o}}{\partial E}) \frac{e}{h} \vec{E}_{z} \frac{\partial \psi}{\partial k_{z}} = (-\frac{\partial f_{o}}{\partial E}) I(\psi) (3.49)$$

Since ψ is linear in \vec{E} , the third term on the left hand side of equation (3.49) is quadratic in \vec{E} and is thus a higher order term. The linearized BTE then becomes,

$$\omega_{c} \frac{\partial \psi}{\partial \phi} - I (\psi) = e \stackrel{\rightarrow}{V} \stackrel{\rightarrow}{\cdot} \stackrel{\rightarrow}{E}$$
 (3.50)

To derive the magnetic field dependences of the leading terms in the transport tensor elements for a general metal, we have to solve equation (3.50) in the high field limit. We begin by expanding ψ_i (i = x,y,z) in a power series in $\frac{1}{H}$.

$$\psi = \sum_{i} \psi_{i} = \sum_{i} \left[\psi_{i}^{(0)} + \left(\frac{1}{H} \right) \psi_{i}^{(1)} + \left(\frac{1}{H} \right)^{2} \psi_{i}^{(2)} + \dots \right]$$
 (3.51)

Note that because the linearity of the BTE, its solutions, $\psi_{\chi},~\psi_{y},$ ψ_{z} are independent of each other.

By substituting equation (3.51) into equation (3.50) and using the fact that $I(\psi)$ is a linear operator, we derive general equations for the $\psi_i^{\ (n)}$ which is the coefficient of the term $(\frac{1}{H})^n$ in the i^{th} component of ψ .

Using the information we obtain, we get expansions of the transport tensor elements in powers of $\frac{1}{H}$, and find, for each tensor element, the leading (non-zero) coefficient for any metal, either compensated or uncompensated, and for open or closed orbits. These coefficients determine the behavior of σ , ρ and ϵ " in the high magnetic field limit. From such calculations in the high-field limit we get the following results (Ref. 56) [In the following pages the ith, jth element of any tensor \star is defined as \star is \star if \star if \star if \star if \star is the magnetic field dependence of the ith, jth element, and \star is its coefficient.]:

The magnetic field dependence of σ in the high field limit in a compensated and uncompensated metal with no open orbits in the x-y plane and the magnetic field in z-direction is

$$\sigma_{\text{uncomp}}^{\leftrightarrow \rightarrow} (H^{\rightarrow \infty}) = \begin{bmatrix} \sigma' x x \frac{1}{H^2} & \sigma' x y \frac{1}{H} & \sigma' x z \frac{1}{H} \\ \sigma' y x \frac{1}{H} & \sigma' y y \frac{1}{H^2} & \sigma' y z \frac{1}{H} \\ \sigma' z x \frac{1}{H} & \sigma' z y \frac{1}{H} & \sigma' z z \end{bmatrix}$$
(3.52a)

$$\overset{\leftarrow}{\sigma}_{\text{comp}}^{(H\to\infty)} = \begin{bmatrix}
\sigma' \times x \frac{1}{H^2} & \sigma' \times y \frac{1}{H^2} & \sigma' \times z \frac{1}{H} \\
\sigma' \times y \frac{1}{H^2} & \sigma' \times y \frac{1}{H^2} & \sigma' \times z \frac{1}{H} \\
\sigma' \times z \times \frac{1}{H} & \sigma' \times z \times \frac{1}{H} & \sigma' \times z
\end{bmatrix}$$
(3.52b)

To evaluate the structure of $\dot{\epsilon}^{"}(H)$, since the Mott Rule applies to each element of $\dot{\sigma}^{"}(H)$, the magnetic field dependence of $\dot{\epsilon}^{"}$ is exactly the same as that for $\dot{\sigma}^{"}$, with the exception that in a

compensated metal the ϵ''_{yx} term retains its $\frac{1}{H}$ power. The magnetic field dependence of ϵ'' in the high field limit for a compensated or uncompensated metal with no open orbits in the plane perpendicular to \hat{H} is thus

$$\frac{\xi}{\varepsilon} = \begin{bmatrix}
\varepsilon' \times x & \frac{1}{H^2} & \varepsilon' \times y & \frac{1}{H} & \varepsilon' \times z & \frac{1}{H} \\
\varepsilon'' \times y \times \frac{1}{H} & \varepsilon' \times y & \frac{1}{H^2} & \varepsilon' \times z & \frac{1}{H} \\
\varepsilon' \times x & \frac{1}{H} & \varepsilon' \times y & \frac{1}{H^2} & \varepsilon' \times z & \frac{1}{H}
\end{bmatrix}$$
(3.53)
$$\frac{\xi}{\varepsilon} = \begin{bmatrix}
\varepsilon' \times x & \frac{1}{H^2} & \varepsilon' \times y & \frac{1}{H^2} & \varepsilon' \times z & \frac{1}{H} \\
\varepsilon' \times x & \frac{1}{H} & \varepsilon' \times y & \frac{1}{H} & \varepsilon' \times z & \frac{1}{H^2} & \varepsilon' \times z & \frac{1}{H^2}
\end{bmatrix}$$

Since the magnetic field dependences of the resistivity tensor elements for compensated metals are very different from those in uncompensated metals, we list the tensor elements ρ for compensated and uncompensated metals as well.

$$\rho_{\text{uncomp}}^{\leftarrow}(H^{\rightarrow}\infty) = \begin{bmatrix}
\rho'_{xx} & \rho'_{xy}H & \rho'_{xz} \\
-\rho'_{yx}H & \rho'_{yy} & \rho'_{yz} \\
\rho'_{zx} & \rho'_{zy} & \rho'_{zz}
\end{bmatrix} (3.54a)$$

The Hall coefficient and the Righi-Leduce coefficient are defined by equations (1.19) and (1.20) and they can be written as

$$R_{H} = \frac{\rho_{yx}}{B} = \frac{1}{\sigma_{yx} \cdot B}$$
 (3.56)

$$R_{L} = \frac{(\partial T/\partial Y)}{Q_{\mathbf{x}} \cdot B} = \frac{1}{\lambda''_{\mathbf{v}\mathbf{x}} \cdot B}$$
 (3.57)

In the high field limit, the off-diagonal components of the electrical and thermal conductivity tensors $\overset{\leftarrow}{\sigma}$ and $\overset{\leftarrow}{\lambda}$ should obey the Wiedeman-Franz law at all temperatures, independent of the nature of the scattering integral (Ref. 2)

$$\frac{\lambda''xy}{\sigma_{xy}} = L_0 \cdot T \tag{3.55}$$

By applying the Weideman-Franz law to the Hall coefficient, the Righi-Leduc coefficient R_L can be evaluated. As described in the introduction, R_L provides a means for evaluating the value of Q_{χ} at the center of the sample, where the NE coefficient is measured.

With this general background, we now turn to the high-field limit of the NE coefficient, which allows ϵ " to be extracted directly.

(3.4) The High Magnetic Field Nernst-Ettingshausen Coefficient:

First we derive the high-field limit of the NE coefficient for a compensated metal. Since for an uncompensated metal the derivation of the high-field limit is similar to that for a compensated metal, we just write the result for a compensated metal. The adiabatic NE coefficient for a compensated metal is defined as (Ref. 3)

$$Q^{a} = \frac{-\overrightarrow{E}_{y}}{\partial T/\partial x}$$
 (3.58)

This coefficient can be written in terms of the transport coefficients as follows.

First, multiply the first equation of the first form of transport equation (3.21), by the resistivity tensor coefficient $\stackrel{\leftarrow}{\rho}$,

$$\stackrel{\leftarrow}{\rho} \cdot \stackrel{\rightarrow}{J} = \stackrel{\leftarrow}{\rho} \cdot \stackrel{\leftarrow}{\sigma} \cdot \stackrel{\leftarrow}{E} + \stackrel{\leftarrow}{\rho} \cdot \stackrel{\leftarrow}{\epsilon"} \cdot (-\stackrel{\rightarrow}{\nabla}T)$$
(3.59)

With the experimental boundary conditions $\vec{J}_x = \vec{J}_y = \vec{J}_z = 0$, and the fact that $\vec{\rho} \cdot \vec{\sigma} = 1$, we get

$$\dot{E} = -\rho \cdot \dot{\epsilon}^{"} \cdot \nabla T \qquad (3.60)$$

Comparing equation (3.58) and (3.60)

$$Q^{a} = \frac{-E_{y}}{\partial T/\partial x} = -(\hat{\rho} + \hat{\epsilon}^{\dagger})_{yx}$$
 (3.61)

The tensor element ρ • ϵ is derived in Appendix A and its (yx) component is,

$$Q^{a} = -(\stackrel{\leftarrow}{\rho} \stackrel{\leftarrow}{\circ} \stackrel{\leftarrow}{\epsilon}^{n})_{yx} = \rho_{yx} \stackrel{\epsilon^{n}}{\epsilon^{n}}_{xx} + \rho_{yy} \stackrel{\epsilon^{n}}{\epsilon^{n}}_{yx} + \rho_{yz} \stackrel{\epsilon^{n}}{\epsilon^{n}}_{zx} +$$

Ş

*97 ***

. . .

$$(\rho_{yx} \epsilon''_{xy} + \rho_{yy} \epsilon''_{yy} + \rho_{yz} \epsilon''_{zy}) \cdot \frac{\overrightarrow{\nabla}T_{y}}{\overrightarrow{\nabla}T_{x}}$$
 (3.62)

To derive $\frac{\vec{\nabla}T}{\vec{\nabla}T}$ in terms of the transport coefficients, let us look at

the second equation of the second form of the transport equation (3.25), and write down its x, y, components with the boundary conditions $\vec{U}_y = \vec{U}_z = 0$, J = 0, and the fact that there is no temperature gradient in z-direction (the direction of the magnetic field)

$$\vec{U}_{X} = -(\lambda''_{XX}\vec{\nabla}T_{X} + \lambda''_{XY}\vec{\nabla}T_{Y})$$
 (3.63a)

$$\vec{U}_{y} = 0 = -(\lambda''_{yx}\vec{\nabla}T_{x} + \lambda''_{yy}\vec{\nabla}T_{y})$$
 (3.63b)

From equation (3.63.b) we immediately get

$$\frac{\nabla T}{\nabla T_{x}} = -\frac{\lambda''yx}{\lambda''yy}$$
 (3.64)

Substituting this equation into equation (3.62), using equations (3.53) and (3.54b) for magnetic field dependences of a compensated metal in the high field limit, and using the fact that the tensor elements of λ^{\dagger} and σ^{\dagger} are related by the Weideman-Franz law, the leading term of the NE coefficient in high-field limit for compensated metals is simply the second term in equation (3.62)

a a
•
:
1
ä
:
;
į
;
•
;
;
:

$$Q_{\text{comp}}^{a}(H+\omega) \rightarrow \varepsilon y_{x}^{p} p_{yy}$$
 (3.65)

With a similar technique, and with the same boundary conditions, the high-field limit of the adiabatic NE coefficient for an uncompensated metal is

$$P^{a}(H \rightarrow \infty) \rightarrow \frac{\varepsilon'' y x^{\rho} y x}{\lambda'' x y}$$
 (3.66)

Notice that in a compensated metal, ρ_{yy} is proportional to H^2 and ϵ''_{yx} is proportional to H^{-1} , consequently the NE coefficient Q^a is proportional to H. Also in an uncompensated metal, since ρ_{yx} is proportional to H, ϵ''_{yx} is proportional to H^{-1} and λ''_{xy} is proportional to H^{-1} , the NE coefficient P^a is again proportional to H.

With these high-field limits of the NE coefficients for compensated and uncompensated metals, let us see how NE measurements at ultra low temperatures can be examined for presence of electron-phonon mass enhancement.

The off diagonal component of the conductivity tensor, σ_{xy} is well understood; and for no open orbits perpendicular to \vec{B} it is found to be (Ref. 56)

$$\sigma_{xy} = \frac{e(n_e - n_h)}{B} + \frac{0}{B^2} + \dots$$
 (3.67)

wher Volum fine ccap

> ieri unco

> > ther

\$1± 1±

er.

,

Ģ.

where n_e and n_h are the number of electron and holes per unit volume, respectively. In an uncompensated metal where $n_e \neq n_h$, the first term in equation (3.67) is the dominant term. For a compensated metal, where $n_e = n_h$, the first term is zero, but its derivative has exactly the same form as we will find for the uncompensated metal (ref. 56).

From equation (3.35) the off-diagonal component of the thermoelectric tensor is

$$\varepsilon''_{yx} = eL_{o}T(\frac{d\sigma_{yx}}{dE})_{E=E_{F}}$$
 (3.68)

Since $\frac{\partial n}{\partial E}$ and $\frac{\partial n}{\partial E}$ have opposite signs, the densities of states due to the electrons and holes are simply additive, and

$$\varepsilon''_{VX} = eL_{O}^{T} N(B^{-1}) + O(B^{-2}).$$
 (3.69)

Here $N(E_{\hat{\mathbf{f}}})$ is the electronic density of states at the Fermi energy, defined as

$$N(E_{f}) = \frac{\partial n_{e}}{\partial E} - \frac{\partial n_{h}}{\partial E}$$
 (3.70)

Consequently, from equations (3.65) and (3.66) we reach the conclusion that the NE coefficient for compensated and uncompensated metals is proportional to products of terms involving ρ_{yy} , ρ_{yx} , and $\lambda_{xy}^{"}$ times $\epsilon_{yx}^{"}$, where from equations (3.35-3.69) $\epsilon_{yx}^{"}$ is proportional to N(E_F). Since ρ_{xy} , ρ_{yy} , and $\lambda_{xy}^{"}$ are unenhanced

(Ref. 56), in each of these two cases any enhancement must enter through $N(E_f)$. In the introduction, we designated $N(E_f)$ by the symbol $N_t(E_f)$ to distinguish it formally from the specific heat density of states $N_c(E_f)$. Various theoretical estimates of $N_t(E_f)$ have been reviewed in the introduction. The latest estimates predict a proportionality to $(1 + \lambda)$ (Ref. 32) or to $(1 + 2/3\lambda)$ (Ref. 30).

Chapter 4

EXPERIMENTAL RESULTS

High magnetic field limit ($\omega_{\text{C}} \cdot \tau >>1$) measurements of the Nernst-Ettingshausen (NE), Hall (R_{H}), and Righi-Leduc (RL) coefficients were taken on pure polycrystalline Aluminum samples in two different temperature ranges. Rough measurements of NE and somewhat more careful measurements of R_{H} were made between 1K and 4.2K, primarily to develop the measuring equipment and techniques needed to extend the experiments to lower temperatures. More careful measurements were taken below 1K, particularly at the single temperature 147mK, which is low enough so that phonon-drag effects on the NE coefficient should be small. 147mK was chosen as the lowest temperature with enough cooling power with the present dilution refrigerator for measuring the NE and R_{L} coefficients with a resolution of 0.5%. In the last part of this chapter we summarize the data and present our conclusion concerning electron-phonon mass enhancement.

(4.1)Temperature range 1K to 4.2K:

(4.1.1) The Hall coefficient (R_H) above 1 K:

The Hall coefficient of Aluminum was measured in a standard Helium cryostat, using a SQUID as shown in Figure (2.11), as a check on the thickness (t) of the thin Aluminum sample. The sample thickness was estimated independently by use of a caliper, and also

by weighing a piece of known length and width and determining it thickness from its known density. These measurements gave the following results.

Technique	Thickness (t) in Meter
Caliper	$(5.1 \pm 0.5) \times 10^{-5} \text{m}$
Weighing	$(5.08 \pm 0.10) \times 10^{-5} \text{m}$
Hall coefficient	$(5.05 \pm 0.10) \times 10^{-5} \text{m}$

In later analysis we use the value $t = 5.08 \pm 0.10 \times 10^{-5} m$.

From resistivity measurements, the RRR of the sample was evaluated, and it was

$$RRR = \frac{R(300K)}{R(4.2K)} = 958 \pm 10 \tag{4.3}$$

(4.1.2) The Nernst-Ettingshausen coefficient above 1K:

The NE coefficient of Aluminum was also roughly measured in the He cryostat at about 3K and magnetic fields of 2-3T. These measurements were made to check our measuring technique and to establish the amount of vibration isolation needed to achieve voltage noise in the 10⁻¹³V range in the presence of a 3T field. We succeeded in achieving the necessary voltage sensitivity in the presence of the field, and found NE values about 5% higher than those reported by Thaler, Fletcher and Bass (ref.3) in 1977. In view of the crudeness of the measurements, this agreement was taken

as sufficiently good to justify going forward with a more precise measuring system on our dilution refrigerator.

For checking our thermometers, at the same time the NE coefficient was measured, the gradient of the temperature in the x-direction was also measured. Then by measuring the amount of heat applied to the sample, the thermal conductance in the x-direction was determined. From the Weidemann-Franz law, the resistance $R_{\chi\chi}$ at Helium temperature was calculated. The value of this resistance was the same as its directly measured value to within a few percent.

(4.2) Measurements at temperatures below 1K:

As mentioned chapter 2, we reached temperatures below 1K by use of a dilution refrigerator. From the cooling power of the dilution refrigerator as a function of temperature, and also the heat required to be sent through the sample for NE measurements, we found the temperature 147mK to be appropriate for our experiments.

(4.2.1) The Hall coefficient (R_H) below 1K

 $R_{\rm H}$ measurements were made at 147mK for a 2 x 10⁻³" thick Aluminum sample in different magnetic fields, with the magnetic field up (+z-direction) and down (-z-direction) in ten different runs. For these measurements, a typical current of 0.5 mA was sent into the reference resistor and 500 μ A through the sample. The SQUID

noise, which was a function of the magnetic field, was about \pm 1.4 x 10^{-13} volts at 10 kG. The Hall voltage for this sample in 10 kG magnetic field was on the order of 10^{-6} volts which was 10^{7} times larger than the SQUID sensitivity. The Hall coefficient approached its saturated theoretical value of $(1.025 \pm 0.005) \times 10^{-10} \text{ m}^3 \text{c}^{-1}$, to within 0.5% above 10 kG. The latest and most reliable sets of data are listed in table (4.1) and a plot of the data as a function of magnetic field is given in Figure (4.1). The thickness of the sample was taken as $5.08 \times 10^{-5} \text{m}$, as discussed above. In Figure (4.1) the broken line is the value of $R_{\text{H}} = 1.023 \times 10^{-10} \text{ m}^3 \text{c}^{-1}$ justified in chapter.1.

Table (4.1) $\rm R_{\mbox{\scriptsize H}}$ for pure Aluminum sample at different magnetic fields and a constant temperature 147 mK.

Run #	Magnetic field	Field direction	$R_{H} = \frac{\rho_{yx}}{B} (m^{3}c^{-1})$
1 2	(5.0)kG (5.0)kG	up down	$\begin{array}{c} (0.905 \pm 0.01) \times 10^{-10} \\ (0.895 \pm 0.01) \times 10^{-10} \end{array}$
6	(8.0)kG	up	$(0.983 \pm 0.01) \times 10^{-10}$
6	(8.0)kG	down	$(0.979 \pm 0.01) \times 10^{-10}$
· 8	(10.0)kG	up	$(1.015 \pm 0.01) \times 10^{-10}$
	(10.0)kG	up	$(1.018 \pm 0.01) \times 10^{-10}$
6	(12.5)kG	up	$(1.019 \pm 0.01) \times 10^{-10}$
5	(12.5)kG	down	$(1.020 \pm 0.01) \times 10^{-10}$
8 5 8 5 8 5 8 5 10 5	(14.0)kG (15.0)kG (16.0)kG (17.5)kG (18.0)kG (20.0)kG (22.0)kG (24.0)kG (25.0)kG (26.0)kG	up down up up down up up up up down up up	$ \begin{array}{c} (1.018 \pm 0.01) \times 10^{-10} \\ (1.017 \pm 0.01) \times 10^{-10} \\ (1.019 \pm 0.01) \times 10^{-10} \\ (1.020 \pm 0.01) \times 10^{-10} \\ (1.020 \pm 0.01) \times 10^{-10} \\ (1.018 \pm 0.01) \times 10^{-10} \\ (1.019 \pm 0.01) \times 10^{-10} \\ (1.017 \pm 0.01) \times 10^{-10} \\ (1.018 \pm 0.01) \times 10^{-10} \\ (1.019 \pm 0.01) \times 10^{-10} \\ \end{array} $
10	(28.0)kG	down	$(1.019 \pm 0.01) \times 10^{-10}$
10	(28.5)kG	up	$(1.020 \pm 0.01) \times 10^{-10}$

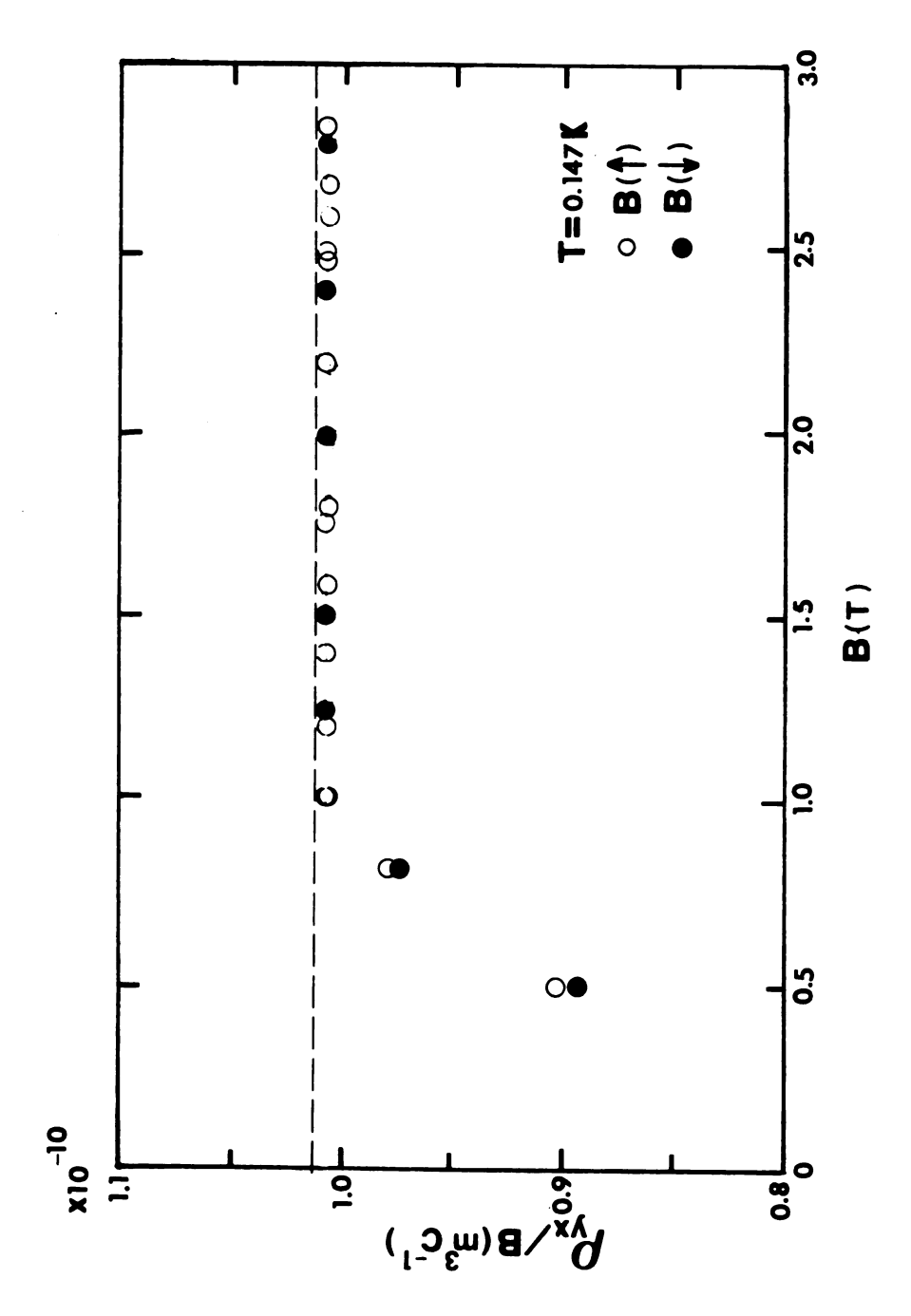


Figure (4-1) Hall coefficient of Al as a function of magnetic field B at temperature, 0.147K. The broken line is the value predicted from the known electronic structure of Al.

(4.2.2) The NE coefficient below 1K:

The NE coefficient of the Aluminum sample was measured with the refrigerator held at 147mK as a function of magnetic field in different runs. Because of the applied temperature gradient, the temperature at the center of the sample was about 210mK. An uncorrected value of the NE coefficient was first determined from equation (1.13). In this equation, $U_{\rm X}$ is the thermal current density:

$$U_{x} = \frac{Q_{x}}{W \cdot t} = \frac{R_{heater} \cdot I_{heater}^{2}}{W \cdot t}$$
 (4.3)

Such uncorrected data from the last few runs, by which time the bugs had been worked out of both the equipment and our measuring procedure, are listed first in table (4.2).

As mentioned in chapter 1, because the sample is very thin, a significant portion of the heat sent into the sample might go through the substrate. In such a case, the Q_{χ} in equation (1.13) would not be exactly equal to $R_h I_h^2$ as assumed in equation (4.3). A value of Q_{χ} corrected for heat flow through the substrate was estimated from R_L measurements on the sample as discussed in chapter 1. The results are given next.

(4.2.3)Correction of $\mathbf{Q}_{\mathbf{X}}$ by $\mathbf{R}_{\mathbf{L}}$ measurements:

The Righi-Leduc coefficient has a high-field limit shown in equation (1.20). From the known value of R_L for Aluminum and the measured value of ∇T_y , the transverse temperature gradient, we calculated Q_x as follows. Combining equations (1.19) and (1.20), Q_x could be deduced from:

$$Q_{X} = \frac{\partial T}{\partial y} \cdot \frac{L_{O}^{T}}{R_{H}B}, \qquad (4.4)$$

where $\frac{\partial T}{\partial y} = \frac{\Delta T}{W}$ is the transverse temperature gradient, and compared with I_X^2R . The ratio of the value determined from equation (4.4) to that determined from I_X^2R determines the fraction of the heat passing through the center of the sample at a given magnetic field. These ratios were difficult to measure reliably, since the typical temperature differences across the sample were only 5-10 mK. Under the best conditions, we could resolve these differences to an uncertainty of 5-10%. In the last run, when we had established our measuring procedures, we measured the heat ratios for an average sample temperature of 0.215K at -16 kG, + 20 kG, again, and - 20 kG. The values found were 104% at -16 kG, 90% at +20 kG, 85% at +20 kG, and 100% at -20 kG, each with an uncertainty of 5-10%. We see that the negative field values were slightly more positive than the positive field values. If we linearly average these four values, so as to eliminate effects of + and - field, we find an

average of 95 + 5%, which we take as the "best" R, correction. Using this correction factor, we calculated the "corrected" values of NE listed second in table 4.2. A plot of Pa/B against B in Figure 4.2 shows that above 8 kG the NE coefficient saturates to a value approximately independent of the magnetic field, until about 21 kG, above which it drops off in value with increasing field. We tentatively attribute this dropoff above 21 kG to the onset of magnetic breakdown, which is known to occur in Al (ref.8) Since the analysis for mass enhancement assumes both high field saturation of the NE coefficient, and no magnetic breakdown, we use the data between 10kG and 20kG for estimation of the presence and size of any such enhancement. When we examine these data, we find that they clearly demonstrate the presence of a mass enhancement, but within are in slightly better agreement with an enhancement of λ_{λ} than with $2/3\lambda_0$, but we cannot rule out $2/3\lambda_0$ to within our experimental uncertainty.

Table (4.2) Nernst-Ettingshausen Coefficient Measurements for Different Values and Direction ("z"-direction and "-z"-direction) of the Magnetic Field from Direct Technique and its Corrected Values from R coefficient Measurements.

Magnetic field	Magnetic field direction	NE (m ³ J ⁻¹) direct measurement	$NE(m^3J^{-1})$ corrected by R_L
(5.0)kG	up	(4.23±0.20)x10 ⁻¹¹	(4.44±0.50)x10 ⁻ 11
(5.0)kG	down	$(3.93+0.20)\times10^{-11}$	(4.13 <u>+</u> 0.50)x10 ⁻¹¹
(7.5)kG	down	(4.79±0.20)×10 ⁻¹¹	(5.04±0.50)x10 ⁻¹¹
(8.0)kG	down	(5.52±0.15)x10 ⁻¹¹	(5.79±0.45)x10 ⁻¹¹
(10.0)kG	up	(5.00±0.15)x10 ⁻¹¹	(5.25±0.45)x10 ⁻¹¹
(10.0)kG	down	(5.42±0.15)x10 ⁻¹¹	$(5.69\pm0.45)\times10^{-11}$
(12.0)kG	down	(5.63±0.11)x10 ⁻¹¹	(5.91±0.40)x10 ⁻¹¹
(14.0)kG	down	(5.77±0.11)x10 ⁻¹¹	(6.06±0.40)x10 ⁻¹¹
(15.0)kG	down	(5.62±0.11)x10 ⁻¹¹	(5.90±0.40)x10 ⁻¹¹
(15.0)kG	up	(5.22±0.11)x10 ⁻¹¹	(5.48 ± 0.40) x10 ⁻¹¹
(16.0)kG	up	(5.22±0.11)x10 ⁻¹¹	$(5.48\pm0.40)\times10^{-11}$
(16.0)kG	down	$(5.85\pm0.11)\times10^{-11}$	$(6.14\pm0.40)\times10^{-11}$
(17.0)kG	up	$(5.60\pm0.11)\times10^{-11}$	(5.88±0.40)x10 ⁻¹¹
(17.5)kG	down	$(5.38\pm0.11)\times10^{-11}$	(5.65±0.40)x10 ⁻¹¹
(18.0)kG	down	(5.55±0.11) x 10 ⁻¹¹	(5.83±0.40)x10 ⁻¹¹
(18.0)kG	up	$(5.31\pm0.11)\times10^{-11}$	$(5.47\pm0.40)\times10^{-11}$
(20.0)kG	down	(5.58±0.11)x10 ⁻¹¹	$(5.86\pm0.40)\times10^{-11}$
(20.0)kG	up	$(5.57\pm0.11)\times10^{-11}$	$(5.85\pm0.40)\times10^{-11}$

(21.5)kG	down	(5.12 ± 0.11) x10 ⁻¹¹	(5.37 <u>+</u> 0.40)x10 ⁻¹¹
(21.0)kG (21.0)kG (21.0)kG	up down up	$(5.05\pm0.10)\times10^{-11}$ $(5.02\pm0.10)\times10^{-11}$ $(5.00\pm0.10)\times10^{-11}$	(5.30 ± 0.40) x10 ⁻¹¹ (5.27 ± 0.40) x10 ⁻¹¹ (5.25 ± 0.40) x10 ⁻¹¹
(22.0)kG (22.0)kG	down up	$(5.52\pm0.10)\times10^{-11}$ $(4.92\pm0.10)\times10^{-11}$	$(5.79\pm0.40)\times10^{-11}$ $(5.17\pm0.40)\times10^{-11}$
(23.0)kG	up	(4.86 ± 0.20) x10 ⁻¹¹	(5.10 ± 0.40) x10 ⁻¹¹
(24.0)kG (24.0)kG	up down	(4.14 ± 0.20) x10 ⁻¹¹ (3.66 ± 0.25) x10 ⁻¹¹	(4.35 ± 0.40) x10 ⁻¹¹ (3.84 ± 0.50) x10 ⁻¹¹
(25.0)kG (25.0)kG	up down	(2.86 ± 0.25) x10 ⁻¹¹ (2.51 ± 0.25) x10 ⁻¹¹	$(3.00\pm0.50)\times10^{-11}$ $(2.63\pm0.50)\times10^{-11}$
(25.5)kG	down	(2.53 ± 0.25) x10 ⁻¹¹	(2.66 ± 0.50) x10 ⁻¹¹
(26.0)kG	up	$(2.15\pm0.25)\times10^{-11}$	(2.26 ± 0.50) x10 ⁻¹¹
(26.5)kG	down	$(2.08\pm0.25)\times10^{-11}$	$(2.18\pm0.45)\times10^{-11}$
(27.0)kG	up	$(1.97\pm0.30)\times10^{-11}$	(2.07 ± 0.50) x10 ⁻¹¹
(27.5)kG	down	(1.65 <u>+</u> 0.30)x10 ⁻¹¹	(1.73 <u>+</u> 0.50)x10 ⁻¹¹

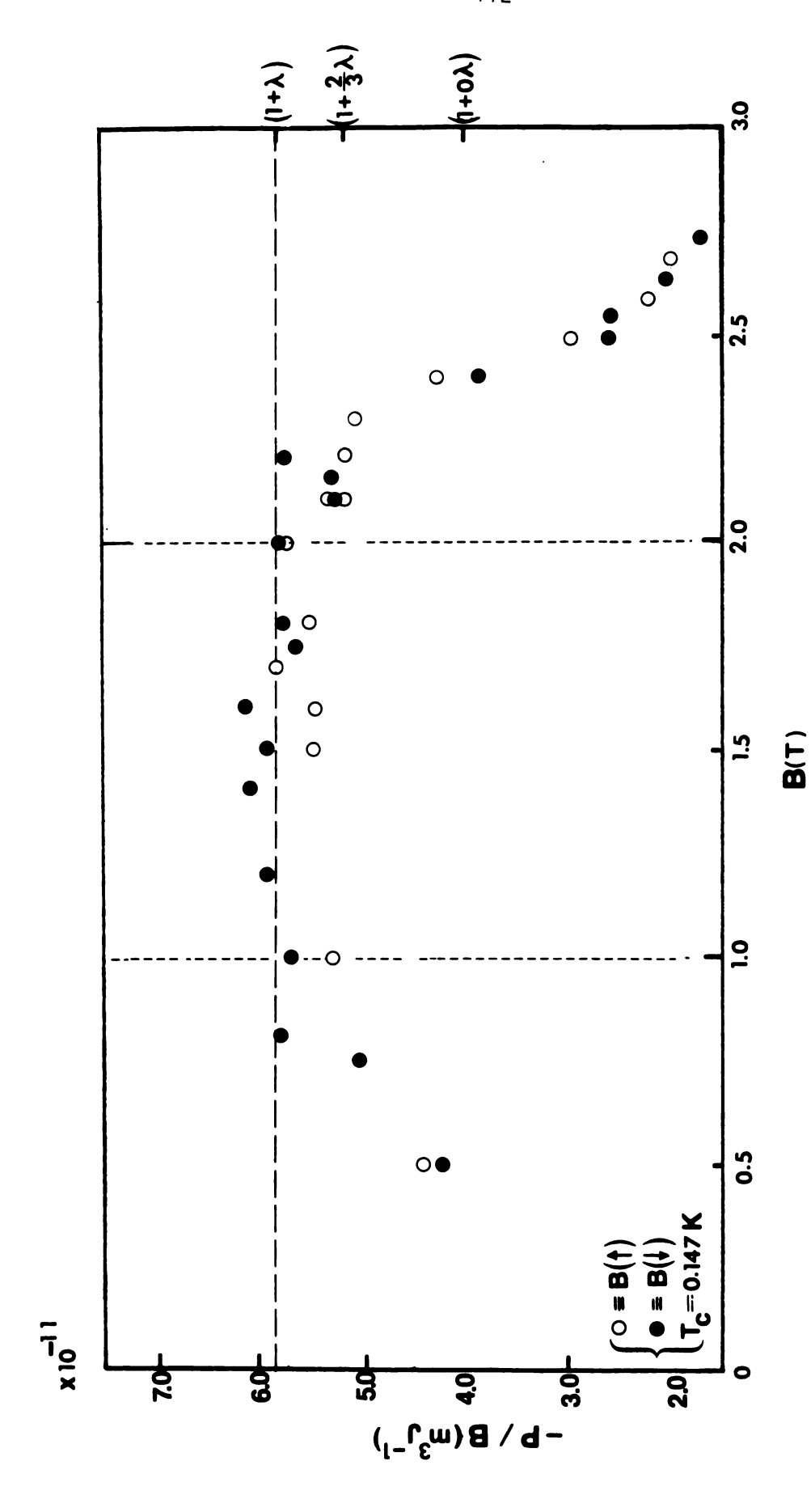


Figure (4-2) NE coefficient as a function of magnetic field at temperature 0.147K. The broken line indicates the value predicted from the electronic specific heat, ζ .

We conclude with a brief demonstration that phonon-drag is unimportant in the NE coefficient at 210mK. The value of the phonon-drag component of the NE coefficient can be estimated from Figure (1.2.b) as follows. In Figure (1.2.b) the intercept at T=0 of $\frac{p^a}{B}$ v.s. T³ is the electron-diffusion component of the NE coefficient. At higher temperatures i.e. 210mK, the phonon-drag component of NE coefficient is just

$$\left(\frac{p^{a}}{B}\right)_{g} = \frac{\partial(p^{a}/B)}{\partial(T^{3})} \cdot (T^{3}) \tag{4.6}$$

From Figure (1.3), $\frac{\partial (p^a/B)}{\partial (T^3)} \sim 1.083 \times 10^{-13} \text{ m}^3 \text{J}^{-1} \text{K}^{-3}$. Therefore the phonon-drag component of NE coefficient at 210mK is

$$\left(\frac{P^a}{B}\right)_g^{T=210mK} \sim 10 \times 10^{-15} \text{ m}^3 \text{J}^{-1} (4.7)$$

This is about 5×10^{-3} times the electron-diffusion component of NE coefficient, and thus considerably smaller than our measuring uncertainty.

(4.3)Conclusion:

We have constructed a system for transport measurements below 1K in magnetic fields up to 30kG, and used it to measure the high magnetic field limit of the Nernst-Ettingshausen coefficient for a pure polycrystalline Aluminum sample at 210mK, where we expect

phonon-drag contributions to be negligible. Previous measurements on Al were limited to above 1.8K. Our data indicate that the electron-phonon mass enhancement continues to appear in the off-diagonal component of the thermoelectric tensor coefficient at temperatures well below 1K. To within our measuring uncertainty, the enhancement in our data between 10 kG and 20 kG is consistent with $(1+\lambda_0)$, in agreement with the low-temperature, high-field NE coefficient measurements of Al from 1.8K to 5K by Thaler, Fletcher and Bass (ref.3). The data are less consistent with an alternative prediction of $(1+2/3\lambda_0)$.

As shown in Figure (4.2), above 20 kG the measured values of the NE coefficient start to drop from the saturated value at lower fields (i.e. between 10 kG and 20 kG). This effect is most likely due to magnetic breakdown in Al above 20 kG. By taking closely spaced data points from 20 kG to 30 kG, we looked for evidence of the quantum oscillations which accompany such breakdown in the thermopower of single crystal samples (ref.8). However, no convincing evidence of such oscillations was found. We assume that their absence is due to the polycrystalline nature of our sample.

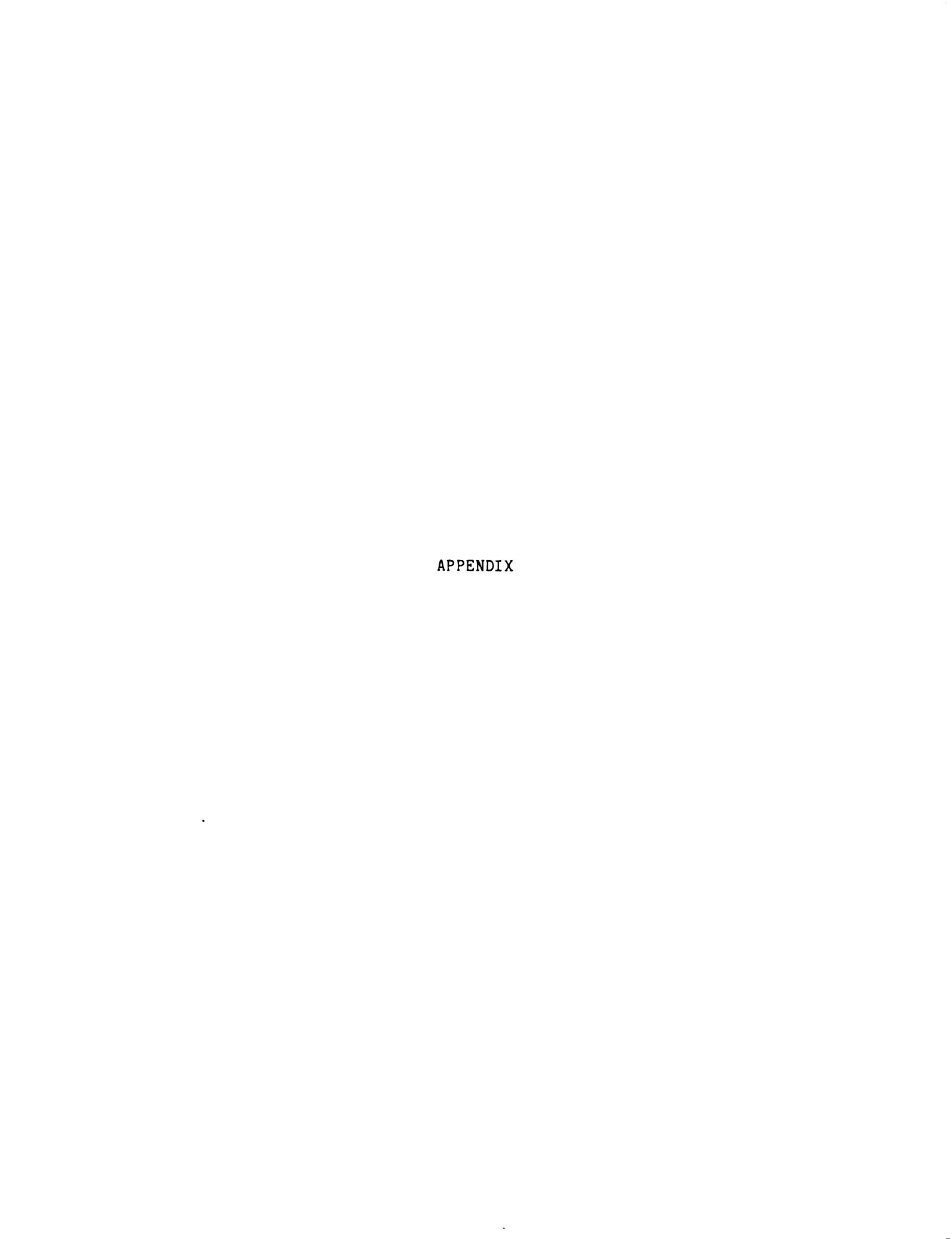


REFERENCES

- 1. B. D. Josephson, Phys. Lett. 1, 251 (1962).
- 2. N. W. Ashcroft and N. D. Mermin, "Solid State Physics" Holt Rinehart Winston (1976).
- 3. B. J. Thaler, R. Fletcher and J. Bass, Journal of Physics: F, Metal Phys. 8,131 (1977).
- 4. J. L. Opsal, Journal of Physics, F: Metal Physics 7, 2349. (1977).
- 5. R. S. Blewer, N. H. Zebouni and C. G. Grenier, Phys. Rev. <u>174</u> 700. (1968).
- 6. J. L. Opsal, B. J. Thaler and J. Bass, Phys. Rev. Lett. <u>36</u>, 1211. (1976).
- 7. R. Fletcher, Phys. Rev. B. 14, 4329. Number 10. (Nov. 1976)
- 8. B. J. Thaler and J. Bass (MSU), Journal of Physics F: Metal Phys. 5, 1554.(1975).
- L. Landau, Z. Eksperim, I. Teor Fiz 30, 1058. (1956) 32, 59. (1957); 35, 97. (1958) [English Transls: Soviet Phys. JETP3.
- 10. R. E. Prange and Leo. P. Kadanoff, Phys. Rev. <u>134</u>, A566. (1964).
- 11. T. Holstein, Ann. Phys. (NY) 29, 410. (1964).
- 12. N. W. Ashcroft and J. W. Wilkins, Phys. Lett. $\underline{14}$, 285. Number 4 (1965).
- 13. C. G. Grenier, K. R. Efferson and J. M. Reynolds, Phys. Rev. 143 (1966).
- 14. R. S. Blewer, N. H. Zebouni and C. G. Grenier, Phys. Rev. <u>174</u> (1968).
- 15. J. R. Long, Phys. Rev. B 3, 1197- (1970).
- 16. R. S. Averback and J. Bass, Phys. Rev. Lett. 26, 882. (1971).
- 17. R. S. Averback, C. H. Stephen and J. Bass, 1973 Journal of Low Temperature Physics 12, 319. (1973).
- 18. R. S. Averback and P. K. Wagner, Solid State Communication, 11, 1109. (1972).

- 19. R. J. Douglas and R. Fletcher, Phil. Mag. 32, 73. (1975).
- 20. R. S. Averback, Ph.D. Thesis, MSU (1971).
- 21. C. K. Chiang, Ph.D. Thesis, MSU (1974).
- 22. R. Fletcher, Phys. Rev. B14, 4329- (1976).
- 23. W. B. Pearson, "A Handbook of Lattice Spacings and Structures of Metals and Alloys", (New York: Pergamon Press) P313, (1958).
- 24. S. K. Lyo, Phys. Rev. Lett, 39, 363. (1977).
- 25. A. Vilenkin and P. L. Taylor, Phys. Rev., 18, 5280. (May 1978).
- 26. A. Vilenkin and P. L. Taylor, Phys. Rev. Lett., <u>42</u>, 597. (Nov. 1978).
- 27. Y. A. Ono and P. L. Taylor, Phys. Rev. B22, 1109 (1980).
- 28. Y. A. Ono, Journal of Phys. F: Metal Phys. 14, L11. (1980).
- 29. J. Friedel, Adv. Phys. 3, 446. (1954).
- 30. J. Rammer and H. Smith, Physics Laboratory I, University of Copenhagen, H. C. Orsted Institute Universitetsparken 5, DK-2100 Copenhagen 0, Denmark. (May 1982).
- 31. L. V. Keldysh, Eksp. Zh. Teor. Fiz. <u>47</u>, 1515 (1964) Sov. Phys. JET, P20,1018. (1965).
- 32. W. Hänsch and G. D. Mahan, Phys. Rev. B. <u>28</u>, 1886. (Febuary. 1984).
- 33. W. Hänsch and G. D. Mahan, Phys. Rev. B. <u>28</u>, 1902. (January 1983).
- 34. W. B. Pearson, "A Handbook of Lattice Spacings and Structures of Metals and Alloys" (New York: Pergamon Press) Page 313 (1958).
- 35. Z. Z. Yu, Ph.D. Thesis, MSU (1984).
- 36. C. W. Lee, Ph.D. Thesis, MSU (1980).
- 37. D. Edmunds, W. P. Pratt and J. A. Rowlands, Rev. Sci. Inst. <u>51</u> 1516 (1980).
- 38. B. D. Joephson, Phys. Lett. 1, 251 (1962).
- 39. H. E. Henrikson, California Institute of Technology, Pasadena, California 91109 (1971).

- 40. W. N. Lawless, Industry (Instrument Society of America, Pittsburg, , 4, 1085. Part 2, Page 1143; L. J. Neuringer and L. G. Rubin, (1975)
- 41. G. Frossati, Journal of Phys. 41, C7-95 (1980).
- 42. M. J. Naughton, S. Dickinson, R. C. Samaratunga, J. S. Brooks and K. P. Martin, Rev. Sci. Instrum. 54, (November 1983).
- 43. Cryocaline 2457 University Avenue, St. Paul, MN. 55114.
- 44. S. Kobayasi, M. Shinohava and K. Ono, "Thermometry using 1/8 W Carbon Resistors in a Temperature Region Around 10.
- 45. W. L. Johnson and A. C. Anderson, Rev. Sci. Instrum. <u>42</u>,1296. (May 1971).
- 46. H. H. Sample, B. L. Brandt and L. G. Rubin, Rev. Sci. Instrum. 53(8), 1129. (Aug. 1982).
- 47. J. R. Clement, E. H. Quinnell, M. C. Steele, R. A. Hein and R. L. Dolecek, Reev. Sci. Instrum. 24, 545 (1953).
- 48. W. C. Black, W. R. Roack Jr. and J. C. Wheatley, Rev. Sci. Instrum. 35, 587 (1963).
- 49. J. R. Thompson and J. O. Thomson, Rev. Sci. Instrum. <u>48</u>, 1713 (1977).
- 50. S. Saito and T. Sato, Rev. Sci. Instrum., 46,1226. (September 1975).
- 51. M. Steinback, P. J. Anthony and A. C. Anderson, Rev. Sci. Instrum.49, 671. (May 1978).
- 52. The Indium Corporation of America, 1676 Lincoln Avenue, Utica, New York, U.S.A.
- 53. R. M. Mueller, C. Buchal, T. Overfsluizen and F. Pobell, Rev. Sci. Instum. 49, 515. (1977).
- 54. J. M. Ziman, Electrons and Phonons (Oxford University Press, Longson, 1960).
- 55. S. K. Lyo, Phys. Rev. Lett. 39, 363 (1977).
- 56. A.A.Abrikosov, "Introduction to the Theory of Normal Metals" Academic Press. New York and London. (1972).
- 57. P. L. Taylor "A. Quantumn Approach to the Solid State" Prentice Hall, New Jersey (1970).



APPENDIX A

From equation (3.60) the Tensor $p \cdot \epsilon^+$ is

$$\begin{bmatrix}
\rho_{xx} & \varepsilon_{xx}^{n} + & \rho_{xx} & \varepsilon_{xy}^{n} + & \rho_{xx} & \varepsilon_{xz}^{n} + \\
\rho_{xy} & \varepsilon_{yx}^{n} + & \rho_{xy} & \varepsilon_{yy}^{n} + & \rho_{xy} & \varepsilon_{yz}^{n} + \\
\rho_{xz} & \varepsilon_{zx}^{n} & \rho_{xz} & \varepsilon_{zy}^{n} & \rho_{xz} & \varepsilon_{zz}^{n}
\end{bmatrix}$$

$$= \begin{bmatrix}
\rho_{xx} & \varepsilon_{xx}^{n} + & \rho_{xy} & \varepsilon_{yy}^{n} + & \rho_{xy} & \varepsilon_{yz}^{n} + \\
\rho_{xz} & \varepsilon_{xx}^{n} + & \rho_{yx} & \varepsilon_{xy}^{n} + & \rho_{yx} & \varepsilon_{xz}^{n} + \\
\rho_{yy} & \varepsilon_{yx}^{n} + & \rho_{yy} & \varepsilon_{yy}^{n} + & \rho_{yy} & \varepsilon_{yz}^{n} + \\
\rho_{yz} & \varepsilon_{zx}^{n} & \rho_{yz} & \varepsilon_{zy}^{n} & \rho_{yz} & \varepsilon_{zz}^{n}
\end{bmatrix}$$

$$= \begin{bmatrix}
\rho_{xx} & \varepsilon_{xx}^{n} + & \rho_{yx} & \varepsilon_{xy}^{n} + & \rho_{yx} & \varepsilon_{xz}^{n} + \\
\rho_{yx} & \varepsilon_{xz}^{n} + & \rho_{yy} & \varepsilon_{yy}^{n} + & \rho_{yy} & \varepsilon_{yz}^{n} + \\
\rho_{yz} & \varepsilon_{xz}^{n} + & \rho_{zy} & \varepsilon_{yy}^{n} + & \rho_{zy} & \varepsilon_{yz}^{n} + \\
\rho_{zy} & \varepsilon_{yz}^{n} + & \rho_{zy} & \varepsilon_{yy}^{n} + & \rho_{zy} & \varepsilon_{yz}^{n} + \\
\rho_{zz} & \varepsilon_{zx}^{n} & \rho_{zz} & \varepsilon_{zy}^{n} & \rho_{zz} & \varepsilon_{zz}^{n}
\end{bmatrix}$$

Consequently, \vec{E}_v is

$$\vec{E}_{y} = (\rho_{yx} \epsilon_{xx}^{"} + \rho_{yy} \epsilon_{yx}^{"} + \rho_{yz} \epsilon_{zx}^{"}) \cdot \vec{\nabla}T_{x} + (\rho_{yx} \epsilon_{xy}^{"} + \rho_{yy} \epsilon_{yy}^{"} + \rho_{yz} \epsilon_{zy}^{"}) \cdot \vec{\nabla}T_{y} + (\rho_{yx} \epsilon_{xz}^{"} + \rho_{yy} \epsilon_{yz}^{"} + \rho_{yz} \epsilon_{zz}^{"}) \cdot \vec{\nabla}T_{z}$$

Since $\nabla T_z = 0$.

$$\frac{\vec{\xi}_{y}}{\vec{\nabla}T_{x}} = \rho_{yx} \epsilon_{xx}^{"} + \rho_{yy} \epsilon_{yx}^{"} + \rho_{yz} \epsilon_{zx}^{"} + \rho_{yz} \epsilon_{xy}^{"} + \rho_{yz} \epsilon_{xy}^{"} + \rho_{yz} \epsilon_{yy}^{"} + \rho_{yz}^{"} + \rho_{yz} \epsilon_{yz}^{"} + \rho_{yz} \epsilon_{yz}^{"} + \rho_{yz}^{"} + \rho_{yz}^{"}$$

